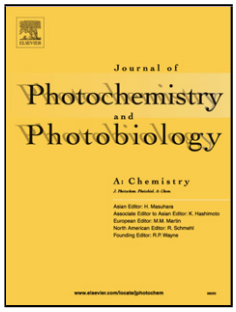

Title: New insights into the rapid deposition and visualization of latent fingerprints: Cyan light emitting $GdAlO_3:Ce^{3+}$ nano fluorescent probe

Authors: C.J. Shilpa, R.B. Basavaraj, G.P. Darshan, H.B. Premkumar, S.C. Sharma, H. Nagabhushana

PII: S1010-6030(18)31599-5
DOI: https://doi.org/10.1016/j.jphotochem.2019.02.027
Reference: JPC 11726

To appear in: *Journal of Photochemistry and Photobiology A: Chemistry*

Received date: 4 November 2018
Revised date: 9 February 2019
Accepted date: 25 February 2019

Please cite this article as: Shilpa CJ, Basavaraj RB, Darshan GP, Premkumar HB, Sharma SC, Nagabhushana H, New insights into the rapid deposition and visualization of latent fingerprints: Cyan light emitting $GdAlO_3:Ce^{3+}$ nano fluorescent probe, *Journal of Photochemistry and amp; Photobiology, A: Chemistry* (2019), https://doi.org/10.1016/j.jphotochem.2019.02.027

New insights into the rapid deposition and visualization of latent fingerprints: Cyan light emitting $GdAlO_3:Ce^{3+}$ nano fluorescent probe

C.J. Shilpa[1], R.B. Basavaraj[1], G. P. Darshan[2], H. B. Premkumar[3], S.C. Sharma[4], H. Nagabhushana[1, *]

[1]Prof. C.N.R. Rao Centre for Advanced Materials Research, Tumkur University, Tumkur 572 103, India
[2]Department of Physics, Acharya Institute of Graduate Studies, Bangalore 560 107, India
[3]Department of Physics, M.S. Ramaiah University of applied Sciences, Bangalore 560 054, India
[4]Director - National Assessment and Accreditation Council (Work carried out as Honorary Professor, Jain University, Bangalore 560 069, India)

Graphical abstract

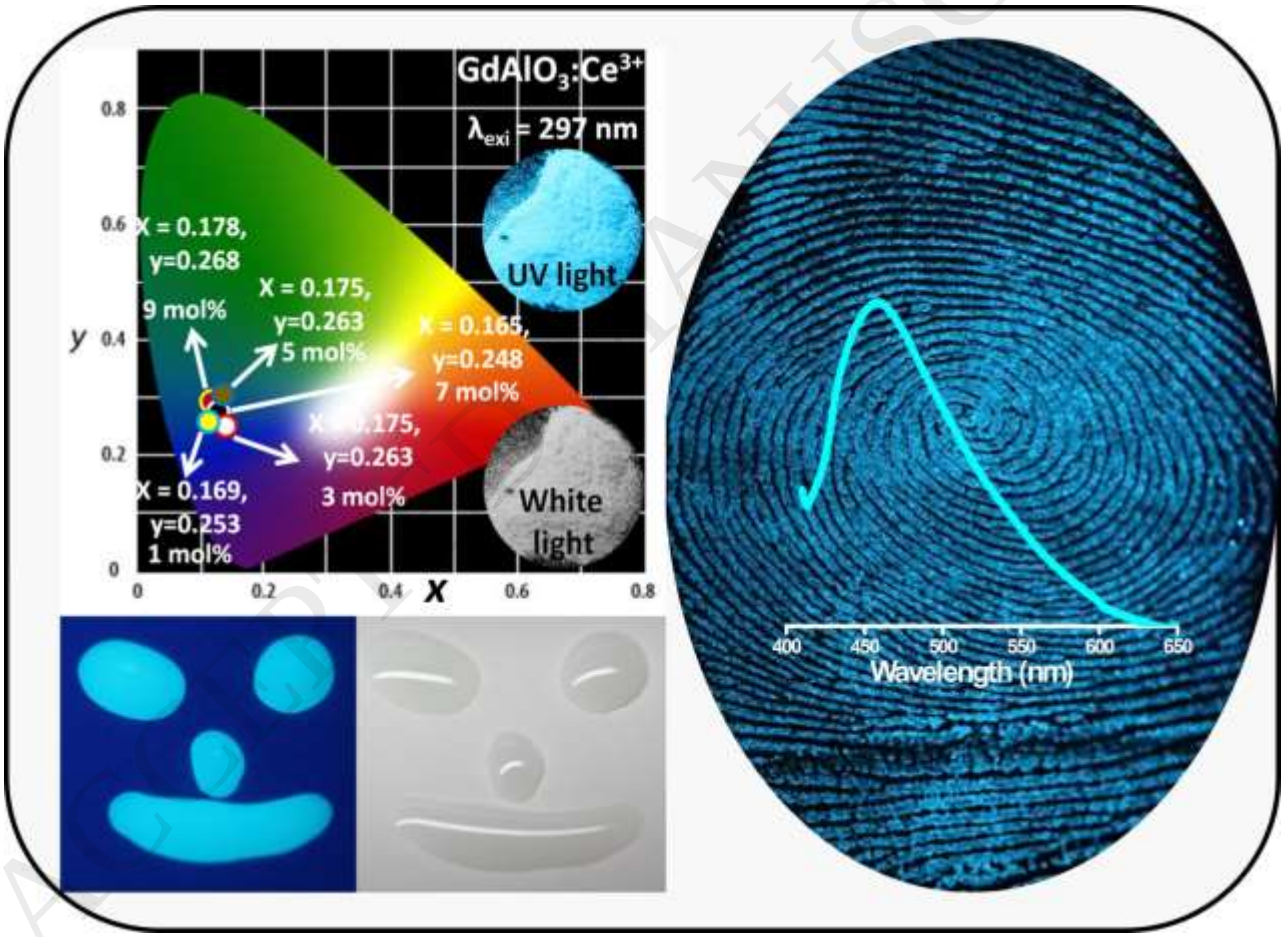

Research Highlights

- Cyan emitting $GdAlO_3:Ce^{3+}$ nanophosphors have been synthesized by solution combustion method.
- The structural, morphological and optical properties of $GdAlO_3:Ce^{3+}$ nanophosphors are analysed.
- The clear visualization results (Type 1-3) of latent fingerprints and anti-counterfeiting labels are developed.

Abstract

The marvelous blend of nanoscience and nanotechnology evoke much interest due to their prospective applications in many fields. They can bridge gap between the nanoscale and microscale world and afford favourable functions. Among various fields, forensic science especially latent fingerprints are the substantial evidences due to their characteristic details and special chemical compositions; hence they serve as identity tool for forensic enquiries as well as medical diagnosis. Therefore, considerable attention was paid by the researchers to visualize latent fingerprints. During visualization, background hindrance from the underlying surface diminishes the visualization sensitivity. Hence, many efforts were attempted to overcome from the background hindrance, but still need to improve. This exciting objective stimulating to fabricate novel $GdAlO_3:Ce^{3+}$ (1-9 mol %) nanophosphors by a facile solution combustion method. The diffraction patterns confirm the orthorhombic phase of the prepared nanophosphors. The photoluminescence emission spectra exhibit a broad peak centered at ~ 466 nm, which attributed to $^5D_{3/2} \rightarrow {}^7F_J$ transitions (J = 7/2 and 5/2) of Ce^{3+} ions. The photometric properties confirm that the prepared samples emit cyan blue color with high color purity. The optimized sample can be used to visualize latent fingerprints with high resolution, sensitivity and less background hindrance. Furthermore, type 1-3 details of latent fingerprints were clearly revealed on various hydrophilic and hydrophobic substrates. These results indicate that the optimized $GdAlO_3:Ce^{3+}$ (5 mol %) nanophosphors were considered as a potential material for latent fingerprints visualization for forensic investigations and anti-counterfeiting applications.

Keywords: Nanophosphor; Photoluminescence; Latent fingerprint; Anti-counterfeiting; Photometric properties.

*Corresponding Author: Dr. H. Nagabhushana (E-mail: bhushanvlc@gmail.com; Tel: +91-966-3177440).

1. Introduction

Fingerprints (FPs) have long been used as powerful physical evidence to identify an individual's unique information [1-3]. FPs have been mostly considered due to its distinguishing profiles, namely ridge flow (level I), core, delta, bifurcation (level II) and sweat pore (level III) that are distinctive in every individual [4]. Hence, FPs are used as a vibrant tool for distinguishing individual statistics in crime scenes. Additionally, latent fingerprints (LFPs) which are invisible to the naked eye, are generally encountered at crime scenes and therefore require a more accurate visualization technique.

Numerous approaches have been explored to visualize LFPs, such as powder dusting, multi-metal deposition (MMD), superglue fuming, fluorescent dyes, etc. Among, powder staining was mostly used visualization method on various surfaces. In order to visualize LFPs many inorganic nanoparticles, specifically Au nanoparticles [5], semiconductor quantum dots [6] and magnetic nanoparticles [7] are well documented. However, elaborate preparation procedures, potential toxicity, destructive nature of visual image and short preservation time typically hindered their wide applications. Therefore, there's still an immediate need for rapid, accurate, efficient and non-destructive material for clear visualization and everlasting steadiness of LFPs [8-10].

Rare earth (RE) ions doped luminescent powders were found to be excellent probes owing to its fast response time, intense brightness, efficiency, etc. [11-16]. As a result, they can be considered as most promising materials for LFPs visualization and anti-counterfeiting applications. Till date, several luminescent powders are used, namely molybdates [17], vanadates [18], silicates [19], aluminates [20] and phosphates [21]. Among, gadolinium aluminate ($GdAlO_3$) was considered to be an excellent host due to its high chemical stability, high melting point, high thermal stability, low thermal expansion, high thermal conductivity and good transparency to infrared radiation [22].

The widespread counterfeiting of currency, paper documents and certificates has become a real threat to society, which may influence on social economy and decrease of monetary value. Thus, anti-counterfeiting of important and valuable items that should not be replicated, such as brands, luxury items, banknotes, tickets, and certificates was huge task for companies, governments and customers around the world [23]. From the past decades, many anti-counterfeiting technologies have been developed, such as magnetic response, plasmonic security labels and luminescence printing [24]. Among these, luminescence printing offers advantages in easy handling, high-throughput and facile design. However, the traditional luminescent materials used in anti-counterfeiting are hazardous to user health due to usage of poisonous solvents and materials. To overcome from these issues, it's necessary to develop luminescent materials with high potency, high distinction, high property and non-toxicity.

In the present work, we report a simple and straightforward technique to synthesize the cyan emitting $GdAlO_3:Ce^{3+}$ (1-9 mol %) nanophosphors (NPs). For the first time we report the use of optimized $GdAlO_3:Ce^{3+}$ (5 mol %) NPs as a novel fluorescent label for completely developing whole LFPs. We successfully used $GdAlO_3:Ce^{3+}$ (5 mol %) NPs to clearly visualize LFPs on various hydrophilic and hydrophobic substrates by powder dusting method.

2. Experimental

2.1. Materials and method

Gadolinium (III) nitrate hexahydrate [$Gd(NO_3)_3 \cdot 6H_2O$; 99.9 % purity], Aluminum nitrate nonahydrate [$Al(NO_3)_3 \cdot 9H_2O$; 99 % purity], Cerium (III) nitrate hexahydrate [$Ce(NO_3)_3 \cdot 6H_2O$; 99.9 % purity] were purchased from Sigma Aldrich, India and are used without further purification. The laboratory made Oxalyl dihydrazide (ODH:$C_2H_6N_4O_2$) was used as a fuel. De-ionized water was obtained using an ultrafiltration system (Milli-Q, Millipore). The stoichiometry of the redox mixture used for the combustion was calculated

using the total oxidizing and reducing valences of the compounds. For the synthesis of $GdAlO_3:Ce^{3+}$ (1-9 mol %) NPs, a solution combustion method was utilized. The blue emitting NPs are fabricated with stoichiometric quantities of the corresponding metal nitrates as well as fuel are dissolved in de-ionized water and stirred for ~ 30 min on a magnetic stirrer to get uniform mixture. The petri dish containing redox mixture was introduced into a muffle furnace maintained at 500 ± 10 ^oC. Initially, the solution boils and undergoes dehydration. Eventually, the mixture gets decomposed, resulting in the liberation of large amounts of gases (usually CO_2, H_2O and N_2). The whole process was completed in less than 5 min and resulted in the formation of highly porous $GdAlO_3:Ce^{3+}$ (1-9 mol %) NPs. Further, the product was calcined for ~ 900 ^oC for ~ 3 h. The balanced chemical reaction assuming complete combustion of the redox mixture used for the synthesis of $GdAlO_3:Ce^{3+}$ NPs may be written as;

$$Gd(NO_3)_3 + Al(NO_3)_3 + 3C_2H_6N_4O_2(ODH) \rightarrow GdAlO_3 + 6CO_2 + 9H_2O + 9N_2 \text{ ------ (1)}$$

$$(1-x)\,Gd(NO_3)_3 + xCe(NO_3)_3 + Al(NO_3)_2 + 3C_2H_6N_4O_2 \rightarrow Gd_{(1-x)}Ce_xAlO_3 + 6CO_2 + 9N_2 + 9H_2O \text{ ------ (2)}$$

2.2. Visualization of latent fingerprints

The LFPs on various hydrophilic (magazine covers, bank notes and credit cards) and hydrophobic (stainless steel, scissor, knife, key, etc.) substrates are collected from various donors. Before stamping the LFPs, the volunteer's hands were washed thoroughly with soap water. Then, the optimized $GdAlO_3:Ce^{3+}$ (5 mol %) NPs was stained on the LFPs with a light brushing action. The excess NPs was removed by dusting the substrate surfaces with a gentle, smooth motion until a FPs image was developed. The developed FPs image were photographed *in situ* using a DSLR Nikon digital camera under 254 nm UV light. Traditionally used powders, such as TiO_2 [21 nm, ≥ 95.5 % purity; Sigma-Aldrich], Fe_2O_3 [< 5 μm, ≥ 96 % purity, Sigma-Aldrich] are utilized for comparison of the developed LFPs.

Fig.1 shows the various steps involved in the synthesis of NPs and LFPs visualization by powder dusting method.

2.3. Fabrication of anti-counterfeiting ink

A standard PVC gold medium (locally fabricated, printing ink manufactured by Commercial Techno Colors, Ram Nagar, Varanasi-221 005, India) was used to disperse the optimized $GdAlO_3:Ce^{3+}$ (5 mol %) NPs. The dispersive medium serves two important purposes, (i) to disperse NPs into the medium without formation of clusters and (ii) for achieving viscosity (3000 micro poise), which provides sticky nature with printing paper. In the present work, a commercially purchased 50 ml PVC gold medium solution and 250 mg of $GdAlO_3:Ce^{3+}$ (5 mol %) NPs were taken in a beaker and sonicated for ~ 1 h to obtain clear and transparent solution. To make a pattern onto paper, we used a dip pen mode of technique for various designs.

2.4. Characterization

The structural properties of the prepared NPs are analyzed with powder X-ray diffractometer (PXRD, Shimadzu 7000) with Cuk_α (1.541 Å) radiation. The morphological properties are examined by using scanning electron microscope (HITACHI-3000) and transmission electron microscopy (HITACHI-7500). The Jobin Yvon Horiba LABRAM-HR-Visible micro Raman system is used for Raman studies with He-Ne laser (~ 632.8 nm) as the source. For PL studies Jobin Yvon Spectrofluorometer Fluorolog-3 is used with 450W Xenon lamp as an excitation source.

3. Results and discussion

In a crime scene, visualization of LFPs on hydrophilic and hydrophobic surfaces are highly difficult due to background hindrance, availability of partial FPs, complex surfaces, etc. [25, 26]. In the present work, we explored the LFPs on numerous hydrophilic substrates, such as magazine cover, bank notes, master card, plastic sheet, etc. stained with optimized $GdAlO_3:Ce^{3+}$ (5 mol %) NPs using powder dusting method (Figs. 2 and 3). Due to the

interaction between substrates surface and the optimized powder, a clear ridge details were obtained. Fig.4 shows the LFPs visualized on several hydrophobic surfaces, such as knife, scissor, key and spatula under 254 nm UV light. The obtained results evident that, type 1 and type 2 ridge details are undoubtedly visualized due to quick physical adsorption of the NPs by sweat and grease present in the FPs residue. Further, to evaluate the efficiency of the blue emitting NPs for visualization of LFPs on aluminum foil surface, conventionally used staining powders, such as Fe_2O_3 and TiO_2 were used as a control (Fig.5 (a & b)). It was noticed that, the conventional powders could not completely develop the FPs on aluminum foil. However, the FPs visualized by the optimized fluorescent powder, the minutiae ridge of the FPs were clearly resolved (Fig. 5 (c)), indicating that the present powder could be used as an efficient powder for the development of LFPs.

Generally, visualized FPs can be classified into three types. Type -1 provides the pattern data (arches, loops and whorls), type -2 describes the minutiae characteristics, (core, bifurcation, delta, bridge, enclosure, island, short ridge, and hook) and type -3 details refer to the form, number, and placement of sweat pores. This information was used only as a reference data where partial/blurry type-2 details available [27].

Fig.6 (a) shows the visualized FPs on the aluminum foil surface by dusting the optimized $GdAlO_3:Ce^{3+}$ (5 mol %) NPs under 254 nm UV light. As evident from the figure, the detailed ridge characteristics, including type 1 (whorl) and type 2 (lake, short and long fork, island, ridge end, bridge, dot and eye) were clearly revealed. In the present case, type-3 details (sweat pores) were undoubtedly observed, which was most adequate information for individualization. The obtained results evident that the optimized NPs reveal more clear information, including type 1-3 with high sensitivity and low background hindrance. The pixel profile of selected portion of the FP was depicted in Fig.6 (b). As can be seen from the

profile, dusted powder loaded only on the ridges (cyan color) owing to its nano sized particles whereas, it was absent in the furrows region.

Development and visualization of LFPs are a vital task on curved surfaces. In the present work, a series of experiments were performed on various curved surfaces, namely soft drink can, pen, spoon, spray bottle, goggle, glass bottle using simple powder dusting technique (Fig.7). Surprisingly, well defined ridge characteristics could be clearly revealed, indicating that prepared NPs were highly useful for the visualization of LFPs on complex surfaces.

Generally, the quality (in terms of sensitivity and resolution) of the LFPs gets diminishes due to evaporation of water and chemical component in the FPs. As a result, the identification of authenticated details (type 1- 3) of FPs after aging was quite a difficult task for the forensic investigators. Hence, we performed aging experiments (up to 30 days) under room temperature condition (Fig.8). As evident from the figure that, the visualization sensitivity gradually decreased with extended aging of the FPs, due to the continuing evaporation of the FPs. However, LFPs aged for up to 30 days could be visualized with well-defined ridges, signifying that sensitivity of the optimized NPs and developed method was sufficient for visualization of aged FPs. Tang et al. developed LFPs after staining with Ag nanoparticles showed unstable and blurred images upon exposure to the moisture [28, 29]. In the present work, the aged FPs showed intense emission with enhanced ridge patterns, indicating that the optimized NPs have stable physical and chemical properties under ambient atmospheric conditions. The superior adhesion to the ridges may be due to the uniform sized nanoparticles. The fresh FP sweat contains 99 % water, several inorganic salts (such as chloride and phosphate), and organic materials (such as amino acids, fatty acids, urea, and polypeptides) [30, 31]. Therefore, the available water, and organic residues adhere to the

NPs. This might be due to the good hydrophilic nature of the $GdAlO_3:Ce^{3+}$ (5 mol %) NPs, which was confirmed by dispersing these materials in aqueous solution.

To determine the efficiency of the prepared NPs, the LFPs on glass surface are maintained at various temperatures (30 to 55 ^oC) for ~ 1 h (Fig.9). It was evident that the detection sensitivity gradually decreases with increased temperature, due to gradual evaporation of biogenic constituents present in LFPs. In addition, LFPs developed on various fruits (apple and banana) and vegetables (garlic) using optimized NPs under UV 254 nm light (Fig.10). The highest visibility was observed on the surface of apple with clear ridge details. The obtained results signify that prepared NPs and followed method was more sufficient for visualization of LFPs on various surfaces.

A preliminary investigation of anti-counterfeiting applications of the prepared NPs was performed by writing various shapes on the white paper by dip pen mode and visualized under normal and UV 254 nm light. The written images showed superior cyan color emission under UV light (Fig.11 (a', b', c', d')) and exhibits high concealment makes these NPs are new outlook for simpler security ink for more reliable anti-counterfeiting applications.

Fig.12 (a) depicts the PXRD profiles of $GdAlO_3:Ce^{3+}$ (1-9 mol %) NPs. All the diffraction patterns are well indexed to pure orthorhombic structure with JCPDS No: 46-0395 [32]. The site substitution of the dopant (Ce^{3+}) can be inferred from the knowledge of percentage difference D_r in ionic radii between doped and substituted ions. The suitable percentage difference in ionic radii must not exceed 30 %. The acceptable percentage difference (D_r) between doped and substituted ions was calculated using the formula;

$$D_r = \frac{Rm(CN) - Rd(CN)}{Rm(CN)} \quad \text{---------- (3)}$$

where CN; coordination number, Rm (CN); ionic radius of host cations and Rd (CN); ionic radius of dopant ion. The estimated value of D_r between Gd^{3+} and Ce^{3+} on six coordinated site was 7 %. This indicates that the dopant Ce^{3+} ions were effectively substituted in Gd^{3+}

sites. The crystallite size (D) of $GdAlO_3:Ce^{3+}$ (1-9 mol %) NPs were estimated using Scherrer's relation and Williamson–Hall (W-H) plot method [33];

$$D = \frac{0.9\lambda}{\beta \cos\theta} \text{----------(4)}$$

$$\frac{\beta \cos\theta}{\lambda} = \frac{1}{D} + \frac{\varepsilon \sin\theta}{\lambda} \text{----------(5)}$$

where λ; wavelength of the X-rays (1.541 Å), β; full width at half maximum value, θ; Bragg's angle, k; the constant which depends on the grain shape (0.90). Fig.12 (b) depicts W-H plots of the prepared $GdAlO_3:Ce^{3+}$ (1-9 mol %) NPs. The estimated 'D' values of Ce^{3+} doped $GdAlO_3$ NPs were listed in Table.1.

Rietveld method was used to estimate the cell parameters using *FULLPROF* suit program by making use of the Pseudo-voigt function. Rietveld refinement of $GdAlO_3:Ce^{3+}$ (5 mol %) NPs was shown in Fig.12 (c). Further, the corresponding Rietveld refined parameters of undoped and $GdAlO_3:Ce^{3+}$ (5 mol %) NPs are listed in Table.2. Packing diagram was established using the obtained unit cell parameters and was shown in Fig.12 (d). The fitted parameters of R_p, R_{wp} and χ^2 are in good agreement with those obtained from PXRD patterns.

SEM studies are performed to analyse the surface morphology of undoped and Ce^{3+} (1-9 mol %) doped $GdAlO_3$ NPs (Fig.13). It was observed from the micrographs that, the product contains roundish pores with large voids due to the rapid gas evolution during combustion. Further, the pores size increases with increase dopant concentration. This type of porous structure with voids was typical features of combustion synthesis due to escaping large amount of gases [34]. The pore structure may be related to the nature of solution combustion synthesis. Similar results were obtained by Kang et al. [35] in combustion synthesized CeO_2 nanopowders.

Fig.14 shows the TEM, HRTEM and SAED pattern of $GdAlO_3:Ce^{3+}$ (5 mol %) NPs. TEM images clearly indicate that the particles were observed to be almost spherical in shape

with size ranging from ~ 68 – 100 nm (Fig.14 (a & b)). Lattice fringes with the inter-planar spacing of ~ 0.33 nm corresponds to the (112) planes were estimated using HRTEM (Fig.14 (c)). The SAED pattern shows several weak Scherrer's rings corresponding to reflections of orthorhombic $GdAlO_3:Ce^{3+}$ sample and also indicates the NPs are highly crystalline nature (Fig.14 (d)). These reflections planes are well matched with PXRD results.

Raman spectra of $GdAlO_3:Ce^{3+}$ (1-9 mol %) NPs was shown in Fig.15. The spectra exhibit strong peaks located at ~ 155, 236, 313, 385, 406, 482 and 657 cm^{-1} [36]. Further, asymmetric mode was shifted towards the lower wavenumber side, indicating that the presence of oxygen defects, phonon confinement and variation in phonon relaxation.

Fig.16 (a) shows the excitation spectrum of undoped $GdAlO_3$ NPs under 496 nm emission wavelength. It can be observed from the figure that, the spectrum consists of two peaks centered at ~ 300 and 361 nm. PL emission spectrum of $GdAlO_3$ NPs excited at 361 nm recorded in the range of 350-525 nm at RT was shown in Fig.16(b). The spectra consist of two prominent peaks centered at ~ 412 and 496 nm, which may due to recombination of photoexcited holes with electrons occupying the singly ionized oxygen vacancies. In addition, PL excitation and emission spectra of $GdAlO_3:Ce^{3+}$ (1-9 mol %) NPs was shown in Fig.16 (c & d). The excitation spectrum exhibits a broad band centered at ~ 297 nm in the range ~ 250-500 nm, which corresponds to transition of $4f^7 \rightarrow 4f^6 5d^1$ of Ce^{3+} ions. The emission spectra excited at ~ 297 nm exhibits an intensive emission band centered at ~ 466 nm (cyan color). The broad band ~ 466 nm can be resolved into two bands centered at ~ 461 nm and 515 nm, which were attributed to $^5D_{3/2} \rightarrow {}^7F_{5/2}$ and $^5D_{3/2} \rightarrow {}^7F_{7/2}$ transitions of Ce^{3+} ions [37, 38], respectively (Inset of Fig.16 (d)). Variation of PL intensity as a function of Ce^{3+} concentration was studied and shown in Fig.16 (e). The highest PL intensity was endorsed up to 5 mol % of Ce^{3+} ions. Further, with increase of Ce^{3+} ion concentration after 5 mol %, the PL intensity diminishes due to concentration quenching. The cause for the concentration

quenching in the present NPs was explained on the basis of critical distance estimated by the Blasse relation [39];

$$R_C = 2\left[\frac{3V}{4\pi X_C N}\right]^{1/3} \text{---------- (6)}$$

where, N; number of cationic sites, V; cell volume and Xc; critical concentration. In the present work, N = 4, V = 207.42 $(Å)^3$ and X_c = 0.05. By making use of these, the value of R_c was estimated and found to be ~ 9.01 Å. The obtained result signifies that the multipolar interaction was major mechanism for concentration quenching in the prepared NPs.

In order to estimate the type of interactions between the Ce^{3+} ion was determined by the following relation;

$$\frac{I}{X} = k\left[1+\beta\,(X)^{Q/3}\right]^{-1} \text{---------- (7)}$$

where X; concentration of Ce^{3+} ions, k and β; constants and *Q* = 6, 8 and 10 for dipole – dipole, dipole – quadrupole and quadrupole – quadrupole interactions, respectively. The logarithmic plot of (*X*) *Vs* (I/*X*) (Fig.16 (f)), which gives a linear line with a slope = - 0.8346 and intercept = 7.1880. The estimated Q value was close to 8, indicating that the dipole – quadrupole interaction was responsible for concentration quenching phenomena.

The CIE (International Commission on Illumination) coordinates of the prepared $GdAlO_3:Ce^{3+}$ (1-9 mol %) NPs was estimated and shown in Fig.16 (g). From the figure, it was evident that the color coordinates were located in the cyan blue region. The correlated color temperature (CCT) was also estimated as described elsewhere [40]. The average CCT was used to define the color temperature of a light source and it was found to be ~ 7501 K. (Fig.16 (h)). Generally, CCT value more than 4500 K was referred to as cool, while below 3200 K considered as warm. Therefore, the present $GdAlO_3:Ce^{3+}$ (1-9 mol %) NPs was efficient cool blue component for the fabrication of white light emitting diodes. In addition, color purity (CP) of the obtained samples was calculated based on the relation suggested

elsewhere [41]. The obtained values of CP of the prepared NPs are given in Table.3. The obtained results specified that color purity was close to 76 %, indicating that the prepared NPs are quite useful in the fabrication of solid state lighting applications.

The property of thermal stability was a vital parameter for phosphor for actual application [42]. Fig.17 (a) shows temperature responded emission spectra of $GdAlO_3:Ce^{3+}$ (5 mol %) NPs under ~ 297 nm excitation. The duration of thermal treatment for PL spectrum at each temperature point was ~ 5 min. As observed in Fig.17 (b), the PL intensities slowly decline with rising temperature, while the PL shape keeps unchanged. The normalized intensity at ~ 303 K and ~ 423 K keeps 100 % and 66 % of its initial value at room temperature, respectively (Fig.17 (b)). The activation energy (E_a) of thermal quenching (~ 0.34 eV) was obtained by the slope for plots of $\ln[(I_o/I_T)-1]$ versus $1/k_BT$ (Fig.17 (c)), which was higher than many reported Ce^{3+} blue phosphors, i.e. β- $NaSrBO_3:Ce^{3+}$ (0.21 eV) [43] and $Ba_5(BO_3)_2(B_2O_5)$: Ce^{3+} (0.19 eV) [44], and confirms the good thermal stability of $GdAlO_3:Ce^{3+}$ (5 mol %) NPs.

The PL lifetime was an important tool which examines the luminescence performance of the phosphor. Fig.17 (d) displays the decay curve of the optimized $GdAlO_3:Ce^{3+}$ (5 mol %) NPs (excited at ~ 297 nm, monitored at ~ 466 nm). The curve can be well fit by a double-exponential function as: $I(t)=I_o+A_1\exp(-t/\tau_1)+A_2\exp(-t/\tau_2)$, where I and I_o ; luminescence intensity at time t and 0. A_1 and A_2 ; constants, t ; time, and τ_1 and τ_2 ; decay times for the exponential components, respectively. Furthermore, the average decay lifetime (τ_{avg}) can be estimated as follows: $\tau_{avg} = (A_1\tau_1^2+ A_2\tau_2^2)/(A_1\tau_1+ A_2\tau_2)$. The average decay lifetime value was estimated and found to 0.683 ms, which was short enough for possible application in displays and lighting region. In addition, the average decay lifetime of $GdAlO_3:Ce^{3+}$ (1-9 mol %) NPs are given in Table.4. As can be seen from the table, the average lifetime values are found to decrease with increase of Ce^{3+} concentration. The decreasing nature was mainly due

to the non-radiative and self-absorption rate of the internally doped ion which increases when the activators cross the critical separation between the activator ions and quenching sites [45].

4. Conclusions

Cyan emitting $GdAlO_3:Ce^{3+}$ (1-9 mol %) NPs were synthesized by solution combustion method using ODH as a fuel. The PXRD results revealed that the obtained powder NPs consisted out of a single-phase orthorhombic structure and it also indicated that the incorporation of the dopants did not affect the crystal structure. Morphological studies clearly indicate that the prepared particles were almost spherical in shape with size ranging from ~ 68 – 100 nm. PL emission spectra exhibit a broad band centered at ~ 466 nm (cyan color). The broad band ~ 466 nm can be resolved into two bands centered at ~ 461 nm and 515 nm, which were attributed to $^5D_{3/2} \rightarrow {}^7F_{5/2}$ and $^5D_{3/2} \rightarrow {}^7F_{7/2}$ transitions of Ce^{3+} ions, respectively. The PL intensity increased up to 5 mol % of Ce^{3+} ions and later diminishes. The decrease of luminescence with increasing Ce^{3+} was related to a self-quenching of the concentration effect. The dipole – quadrupole interaction was responsible for concentration quenching phenomena. The photometric properties evident that the color coordinates were located in the cyan blue region with ~ 76 % of color purity. LFPs visualized using prepared NPs evidently revealed sharp ridge characteristics with type 1-3 details, indicating that the optimized $GdAlO_3:Ce^{3+}$ (5 mol %) NPs acts as an efficient medium in order to visualize the LFPs due to its nano regime and high luminescence intensity. Aforementioned results evident that the prepared NPs are explored as a multifunctional material in various fields, including forensic, anti-counterfeiting and solid state lighting applications.

References

[1]. S.J. Park, J.Y. Park, H.K. Yang, Luminescence of a novel cyan emitting $Sr_{10}(PO_4)_6O:Ce^{3+}$ phosphor for visualization of latent fingerprints and anti-counterfeiting applications, Sens. Actuators B: Chem., 262 (2018) 542-554.

[2]. P. Hazarika, D. A. Russell, Advances in fingerprint analysis, Angew. Chem., Int. Ed., 51 (2012) 3524.

[3]. A.K. Jain, J. Feng, Latent fingerprint matching, IEEE Trans. Pattern Anal. Mach. Intell., 33 (2011) 88.

[4]. C. Champod, C.J. Lennard, P. Margot, M. Stoilovic, Fingerprints and Other Ridge Skin Impressions, CRC Press, Boca Raton, FL 2004.

[5]. H.W. Tang, W. Lu, C.M. Che, K.M. Ng, Gold nanoparticles and imaging mass spectrometry: Double imaging of latent fingerprints, Anal. Chem., 82 (2010) 1589-1593.

[6]. G.P. Darshan, H.B. Premkumar, H. Nagabhushana, S.C. Sharma, B. Daruka Prasad, S.C. Prashantha, R.B. Basavaraj, Superstructures of doped yttrium aluminates for luminescent and advanced forensic investigations, J. Alloys Compd., 686 (2016) 577-587.

[7]. O.S. Wolfbeis, Nanoparticle-enhanced fluorescence imaging of latent fingerprints reveals drug abuse, Angew. Chem., Int. Ed., 48 (2009) 2268-2269.

[8]. M. Dhanalakshmi, R.B. Basavaraj, G.P. Darshan, S.C. Sharma, H. Nagabhushana, Pivotal role of fluxes in $BaTiO_3:Eu^{3+}$ nano probes for visualization of latent fingerprints on multifaceted substrates and anti-counterfeiting applications, Microchem. J. 145 (2019) 226-234.

[9]. G.P. Darshan, H.B. Premkumar, H. Nagabhushana, S.C. Sharma, S.C. Prashanth, B. Daruka Prasad, Effective fingerprint recognition technique using doped yttrium aluminate nanophosphor material, J. Coll. Inter. Sci., 464 (2016) 206-218.

[10]. A. Sandhyarani, M.K. Kokila, G.P. Darshan, R.B. Basavaraj, B. Daruka Prasad, S.C. Sharma, T.K.S. Lakshmi, H. Nagabhushana, Versatile core-shell $SiO_2@SrTiO_3:Eu^{3+}$, Li^+ nanopowders as fluorescent label for the visualization of latent fingerprints and anti-counterfeiting applications, Chem. Eng. J., 327 (2017) 1135-1150.

[11]. K.N. Venkatachalaiah, H. Nagabhushana, G.P. Darshan, R.B. Basavaraj, B. Daruka Prasad, Novel and highly efficient red luminescent sensor based $SiO_2@Y_2O_3:Eu^{3+}$, M^+ (M^+ = Li, Na, K) composite core–shell fluorescent markers for latent fingerprint recognition, security ink and solid state lightning applications, Sens. Actuators B: Chem., 251 (2017) 310-325.

[12]. R.B. Basavaraj, H. Nagabhushana, G.P. Darshan, B. Daruka Prasad, M. Rahul, S.C. Sharma, R. Sudaramani, K.V. Archana, Red and green emitting CTAB assisted $CdSiO_3$: Tb^{3+}/Eu^{3+} nanopowders as fluorescent labeling agents useful for forensic and display applications, Dyes Pigm., 147 (2017) 364-377.

[13]. B.L. Narayana, Y.K.C. Rangaiah, M. A. Khalid, Study of fingerprint patterns in relation to gender and blood group, J. Evolution Med. Dent. Sci., 5 (2016) 630-633.

[14]. R. Naik, B.R.A. Mujib, N. Telagi, J. Hallur, Comparative analysis of lip with thumbprints: An identification tool in personal authentication, J. Oral Maxillofac. Pathol., 21 (2017) 171-175.

[15]. N.M. Egli Anthonioz, C. Champod, Evidence evaluation in fingerprint comparison and automated fingerprint identification systems—Modeling between finger variability, Forensic Sci. Int., 235 (2014) 86-101.

[16]. Y. Li, L. Xu, B. Su, Aggregation induced emission for the recognition of latent fingerprints, Chem. Commun., 48 (2012) 4109-4111.

[17]. C.S. Lim, A. S. Aleksandrovsky, M. S. Molokeev, A. S. Oreshonkov, V. V. Atuchin, Microwave synthesis and spectroscopic properties of ternary scheelite-type molybdates phosphors NaSrLa(MoO4)3:Er^{3+},Yb^{3+}, J. Alloy. Compd., 713 (2017) 156-163.
[18]. S. W. Kim, T. Hasegawa, M. Muto, A. Toda, T. Kaneko, K. Sugimoto, K. Uematsu, T. Ishigaki, K. Toda, M. Sato, J. Koide, M. Toda, Y. Kudo, Improvement of luminescence properties of rubidium vanadate, RbVO3, phosphors by erbium doping in the crystal lattice, New J. Chem., 41 (2017) 4788-4792
[19]. Z. Tang, D. Wang, W. U. Khan, S. Du, X. Wang, Y. Wang, Novel zirconium silicate phosphor $K_2ZrSi_2O_7$:Eu^{2+} for white light-emitting diodes and field emission displays, J. Mater. Chem. C, 4 (2016) 5307-5313.
[20]. R.V. Yadav, R. S. Yadav, A. Bahadur, S.B. Rai, Down shifting and quantum cutting from Eu^{3+}, Yb^{3+} co-doped $Ca_{12}Al_{14}O_{33}$ phosphor: a dual mode emitting material, RSC Adv., 6 (2016) 9049-9056.
[21]. G.P. Darshan, H.B. Premkumar, H. Nagabhushana, S.C. Sharma, S.C. Prashantha, H.P. Nagaswarupa, B. Daruka Prasad, Blue light emitting ceramic nano-pigments of Tm^{3+} doped $YAlO_3$: Applications in latent finger print, anti-counterfeiting and porcelain stoneware, Dyes Pigm., 131 (2016) 268-281.
[22]. R.K. Tamrakar, K. Upadhyay, M. Sahu, Spectral characterization of Er^{3+}, Yb^{3+} co doped $GdAlO_3$ phosphor prepared by solid state reaction method, J. Alloy. Compd., 689 (2016) 702-712.
[23]. J. Kai, L. Zhang, J. Lu, C. Xu, C. Cai, H. Lin, Triple-mode emission of carbon dots: Applications for advanced anti-counterfeiting, Angew. Chem., 55 (2016) 1-6.
[24]. H. Kang, J.W. Lee, Y. Nam, Inkjet-printed multi-wavelength thermo-plasmonic images for anti-counterfeiting applications, ACS Appl. Mater. Interfaces, 10.1021/acsami.7b19342.
[25]. Y. Kim, H. Jung, J. Lim, S. Ryu, J. Lee, Rapid imaging of latent fingerprints using biocompatible fluorescent Silica nanoparticles, Langmuir, 32 (2016) 8077-8083.
[26]. H. Chen, K. Chang, X. Men, K. Sun, X. Fang, C. Ma, Y. Zhao, S. Yin, W. Qin, C.F. Wu, Covalent patterning and rapid visualization of latent fingerprints with photo-cross-linkable semiconductor polymer dots, ACS Appl. Mater. Interfaces, 7 (2015) 14477-14484.
[27]. M. Dhanalakshmi, H. Nagabhushana, G.P. Darshan, R.B. Basavaraj, B. Daruka Prasad, Sonochemically assisted hollow/solid $BaTiO_3$:Dy^{3+} microspheres and their applications in effective detection of latent fingerprints and lip prints, J. Sci.: Adv. Mater. Devices, 2 (2017) 22-23.
[28]. H.-W. Tang, W. Lu, C.-M. Che, K.-M. Ng, Gold nanoparticles and imaging mass spectrometry: Double imaging of latent fingerprints, Anal. Chem., 82 (2010) 1589-1593.
[29]. Y. He, L. Xu, Y. Zhu, Q. Wei, M. Zhang, B. Su, Immunological multimetal deposition for rapid visualization of sweat fingerprints, Angew. Chem., 53 (2014) 12609-12612.
[30]. J. Liu, Z. Shi, Y. Yu, R. Yang, S. Zuo, Water-soluble multicolored fluorescent CdTe quantum dots: Synthesis and application for fingerprint developing, J. Colloid Interface Sci., 342 (2010) 278-282.
[31]. W. Wang, X. Lei, Z. Ye, N. Zhao, H. Yang, The luminescent properties and latent fingerprint identification application of AlN:Ce, Tb phosphors, J. Alloys Compd., 705 (2017) 253-261.
[32]. C.J. Shilpa, Akila Kadgathur Jayaram, N. Dhananjaya, H. Nagabhushana, S.C. Prashantha, D.V. Sunitha, S.C. Sharma, C. Shivakumara, B.M. Nagabhushana, $GdAlO_3$:Eu^{3+}:Bi^{3+} nanophosphor: Synthesis and enhancement of red emission for WLEDs, Spectrochim. Acta Part A, 133 (2014) 550-558.

[33]. R.B. Basavaraj, H. Nagabhushana, B. Daruka Prasad, S.C. Sharma, K.N. Venkatachalaiah, Mimosa pudica mediated praseodymium substituted calcium silicate nanostructures for white LED application, J. Alloys Compd., 690 (2017) 730-740.

[34]. B. Umesha, B. Eraiah, H. Nagabhushana, S.C. Sharma, B.M. Nagabhushana, C. Shivakumara, J.L. Rao, R.P.S. Chakradhar, Structural, EPR, optical and Raman studies of Nd_2O_3:Cu^{2+} nanophosphors, Spectrochim. Acta, Part A, 94 (2012) 365-371.

[35]. Wooram Kang, Derya Oncel Ozgur, Arvind Varma, Solution Combustion Synthesis of High Surface Area CeO_2 Nanopowders for Catalytic Applications: Reaction Mechanism and Properties, ACS Appl. Nano Mater., 1 (2018) 675-685.

[36]. Anastasia Chopelas, Single-crystal Raman spectra of $YAlO_3$ and $GdAlO_3$: comparison to several orthorhombic ABO_3 perovskites, Phys. Chem. Min., 38 (2011) 709-726.

[37]. J. Zhou, Z. Xia, M. Yang, K. Shen, High efficiency blue-emitting phosphor: Ce^{3+}-doped $Ca_{5.45}Li_{3.55}(SiO_4)_3O_{0.45}F_{1.55}$ for near UV-pumped light-emitting diodes, J. Mater. Chem., 22 (2012) 21935.

[38]. H. Zhang, H. Zhang, W. Liu, Y. Liu, B. Lei, J. Deng, J. Zhang, S. Yan, H. Kuang, J. Zand, Photoluminescence properties and energy transfer between activators at different crystallographic sites in Ce^{3+} doped $Sr_2MgAl_{22}O_{36}$, Ceram. Int., 42 (2016) 16659-16665.

[39]. G. S. R. Raju, J. Y. Park, G. P. Nagaraju, E. Pavitra, H. K. Yang, B. K. Moon, J. S. Yu, Y. S. Huh, J. H. Jeong, Evolution of $CaGd_2ZnO_5$:Eu^{3+} nanostructures for rapid visualization of latent fingerprints, J. Mater. Chem. C, 5 (2017) 4246-4256.

[40]. Publication CIE no 17.4 (1987) International Lighting Vocabulary, Central Bureau of the Commission Internationale de L 'Eclairage, Vienna, Austria.

[41]. A.K. Bedyal, Vinay Kumar, H.C. Swart, Charge compensated derived enhanced red emission from $Sr_3(VO_4)_2$:Eu^{3+} nanophosphors for white light emitting diodes and flat panel displays, J. Alloys Compd., 709 (2017) 362-372.

[42]. Zhenpeng Zhu, Zishan Sun, Ziying Guo, Xinguo Zhang, Luminescence of $Ca_3ZrSi_2O_9$: Ce^{3+} blue phosphor with good thermal Stability, J. Lumin., 207 (2019) 430-434.

[43]. H. Yi, L. Wu, L. Wu, L. Zhao, Z. Xia, Y. Zhang, Y. Kong, J. Xu, Crystal structure of high-temperature phase β-$NaSrBO_3$ and photoluminescence of β-$NaSrBO_3$: Ce^3, Inorg. Chem., 55 (2016) 6487-6495.

[44]. H. Zhang, H. Zhang, Y. Liu, J. Deng, B. Lei, L. Liu, H. Luo, X. Bai, A novel blue emitting $Ba_5(BO_3)_2(B_2O_5)$ Ce^{3+} phosphor for application in near-UV white LEDs, J. Alloys Compd., 688 (2016) 1225-1232.

[45]. K. Mondal, J. Manam, Enhancement of photoluminescence in Eu^{3+} co-activated $Ca_2MgSi_2O_7$:Dy^{3+} phosphors for solid state lighting application, J. Mol. Struct., 1125 (2016) 503-513.

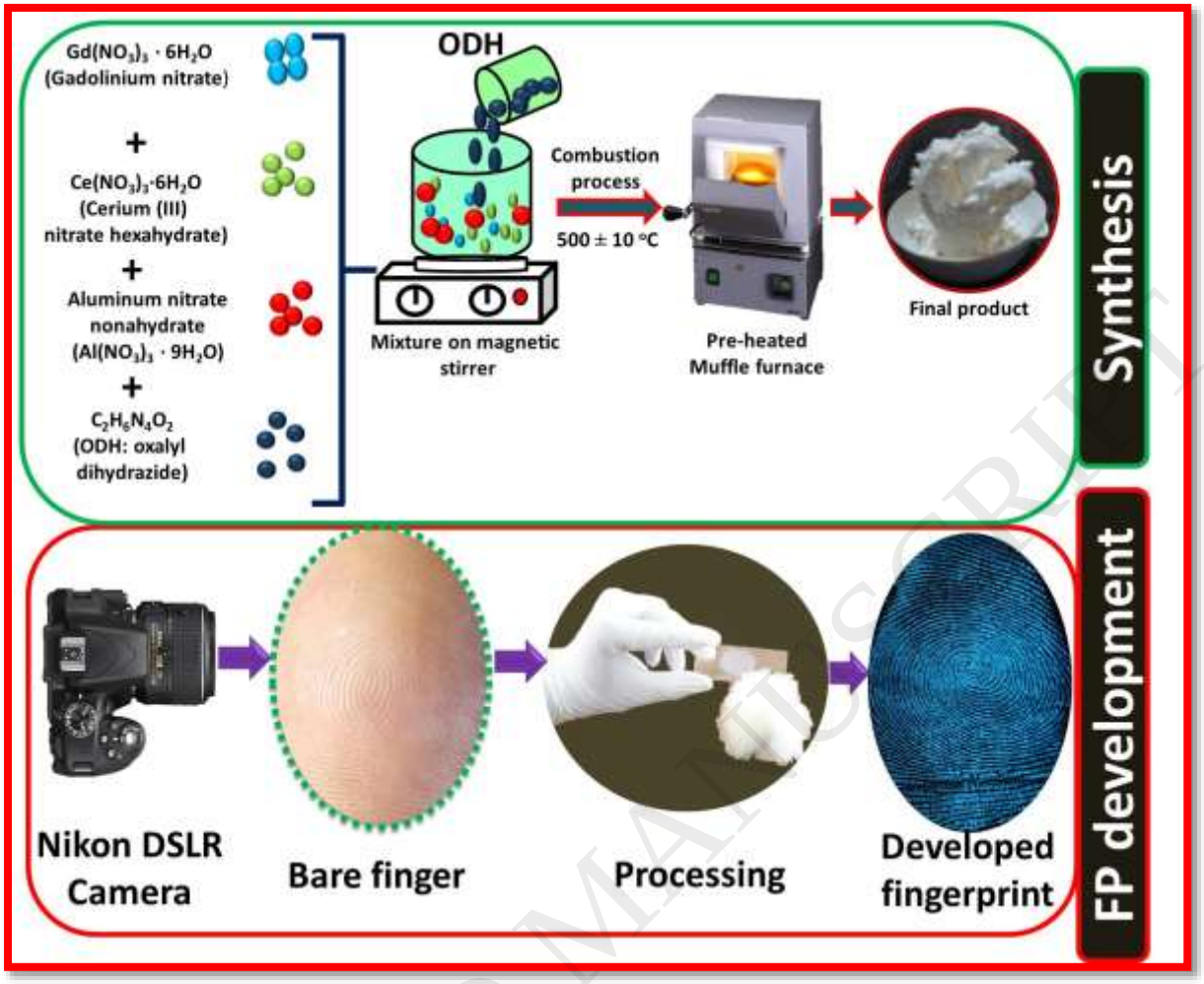

Fig.1. Schematic representation of various step involved in the synthesis of $GdAlO_3:Ce^{3+}$ (1-9 mol %) NPs and LFPs visualization by powder dusting method.

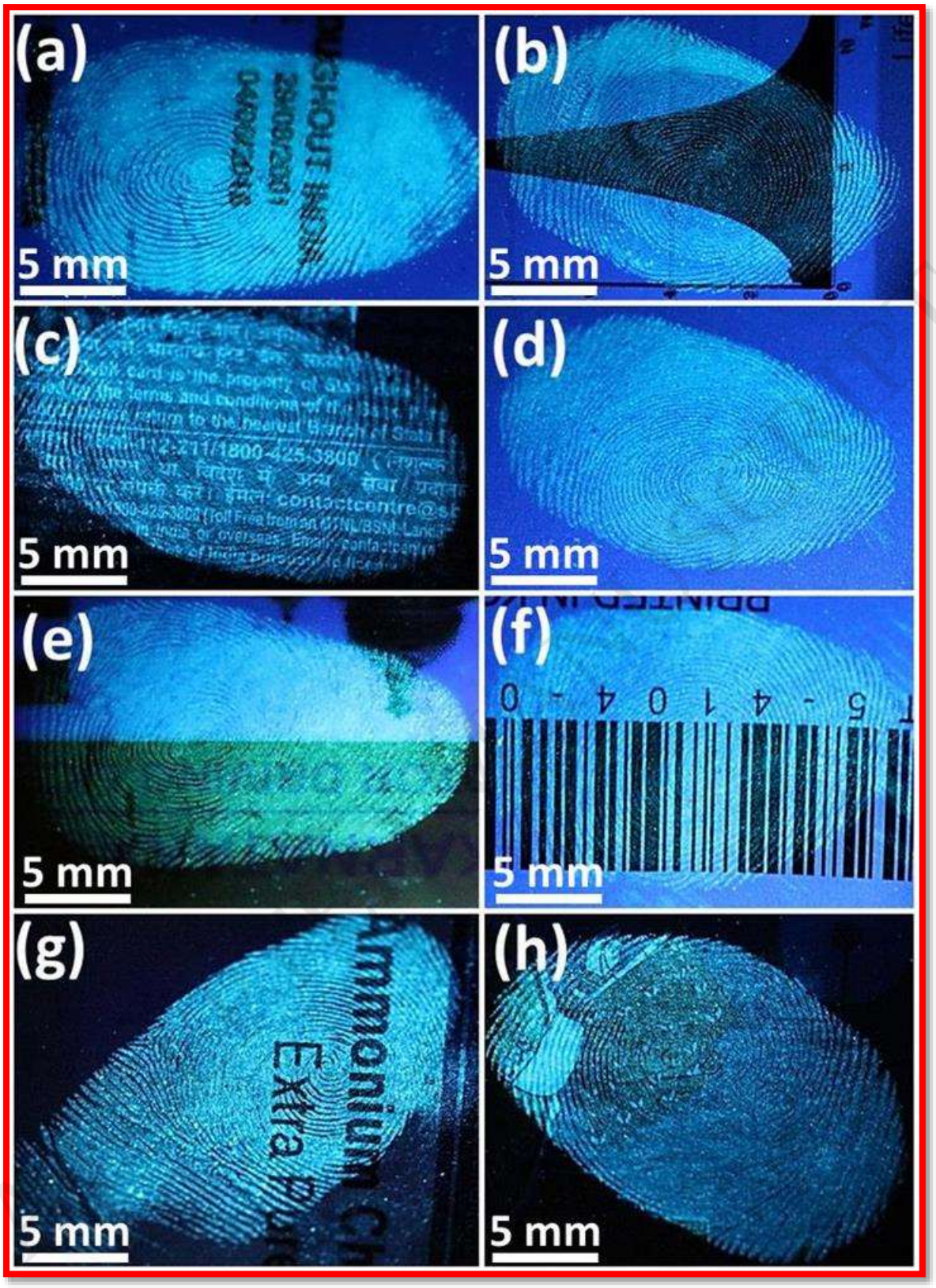

Fig.2. Digital photographs of LFPs visualized by using $GdAlO_3:Ce^{3+}$ (5 mol %) NPs on various hydrophilic surfaces under UV 254 nm light.

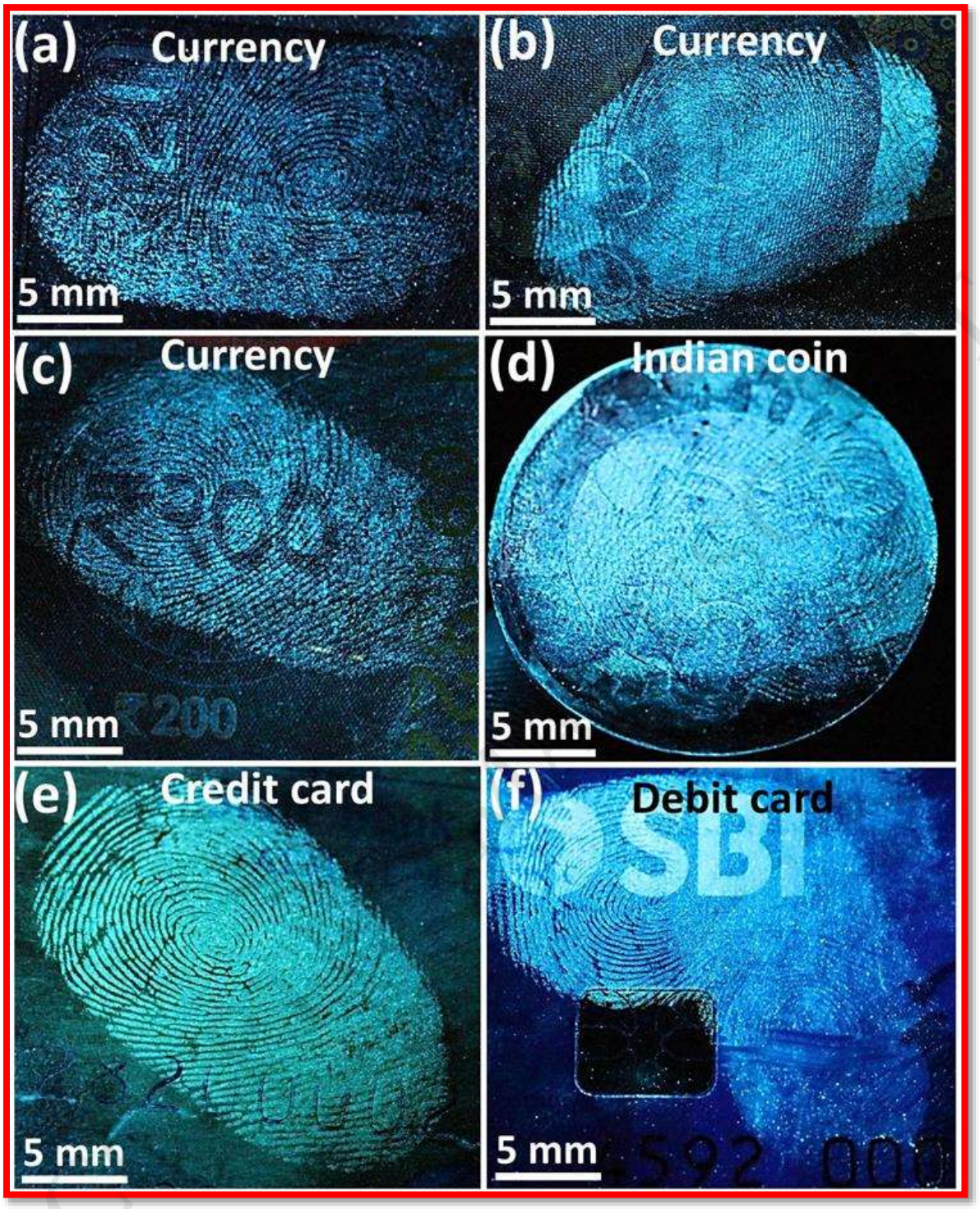

Fig.3. LFPs visualized by using $GdAlO_3:Ce^{3+}$ (5 mol %) NPs on various hydrophilic and hydrophobic surfaces following powder dusting method.

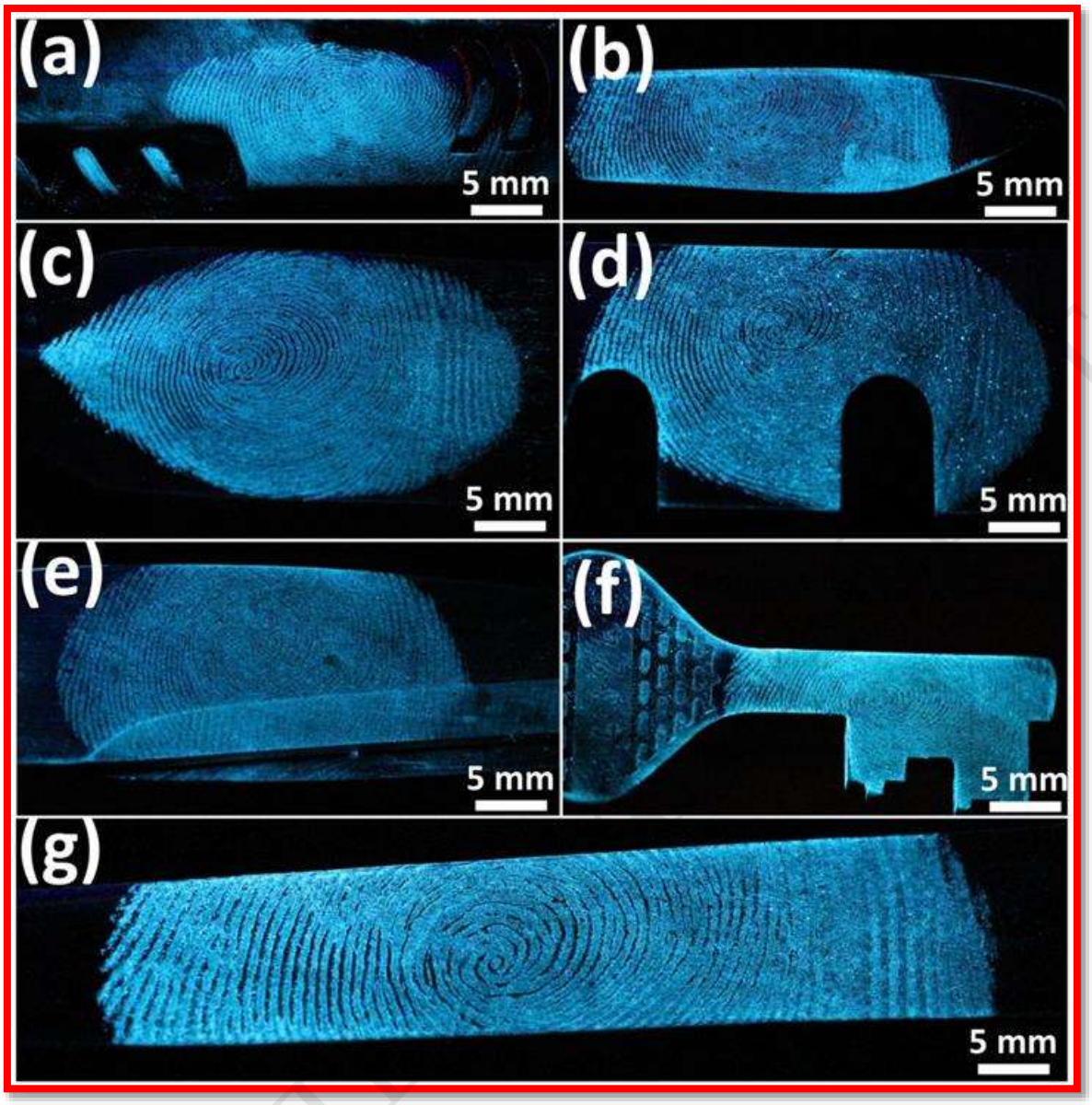

Fig.4. LFPs visualized by $GdAlO_3:Ce^{3+}$ (5 mol %) NPs on various hydrophobic surfaces followed by powder dusting technique.

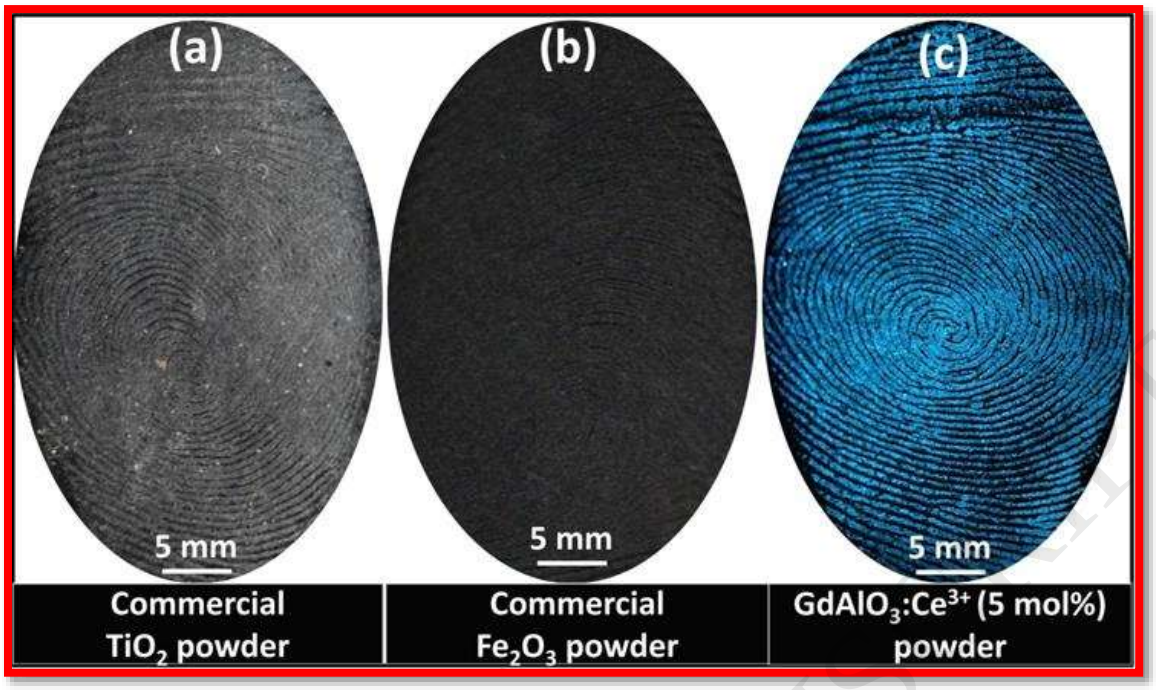

Fig.5. Comparison of LFPs visualized using commercial non-fluorescent powders with optimized $GdAlO_3:Ce^{3+}$ (5 mol %) NPs on aluminum foil surface.

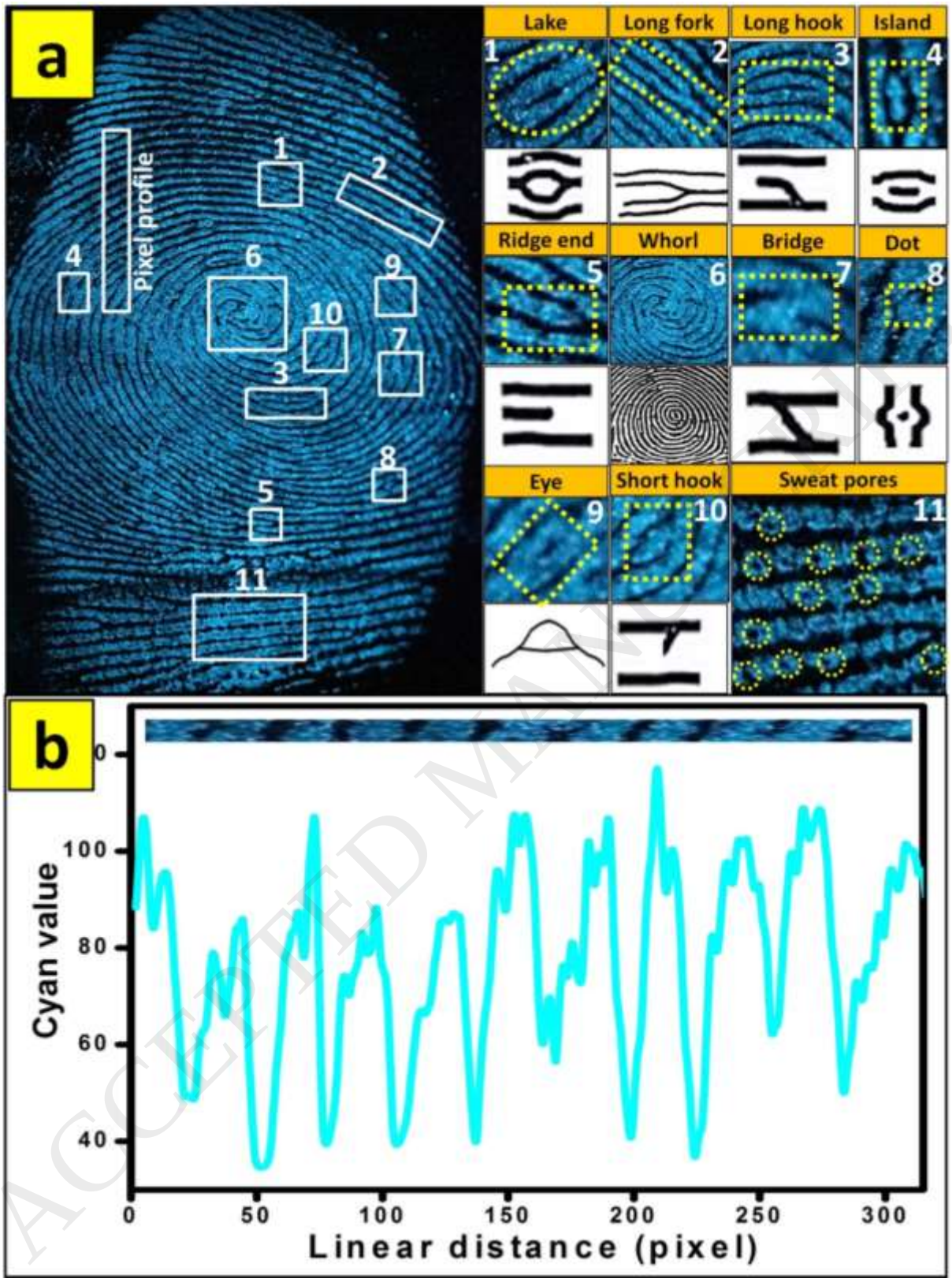

Fig.6 (a) Digital photographs of LFPs microstructures (including type I-III) visualized by $GdAlO_3:Ce^{3+}$ (5 mol %) NPs on aluminum foil surface and (b) fluctuations of cyan value with ridge (cyan) and furrow (black) over a few papillary ridges indicated by rectangle line shown in Fig.6 (a).

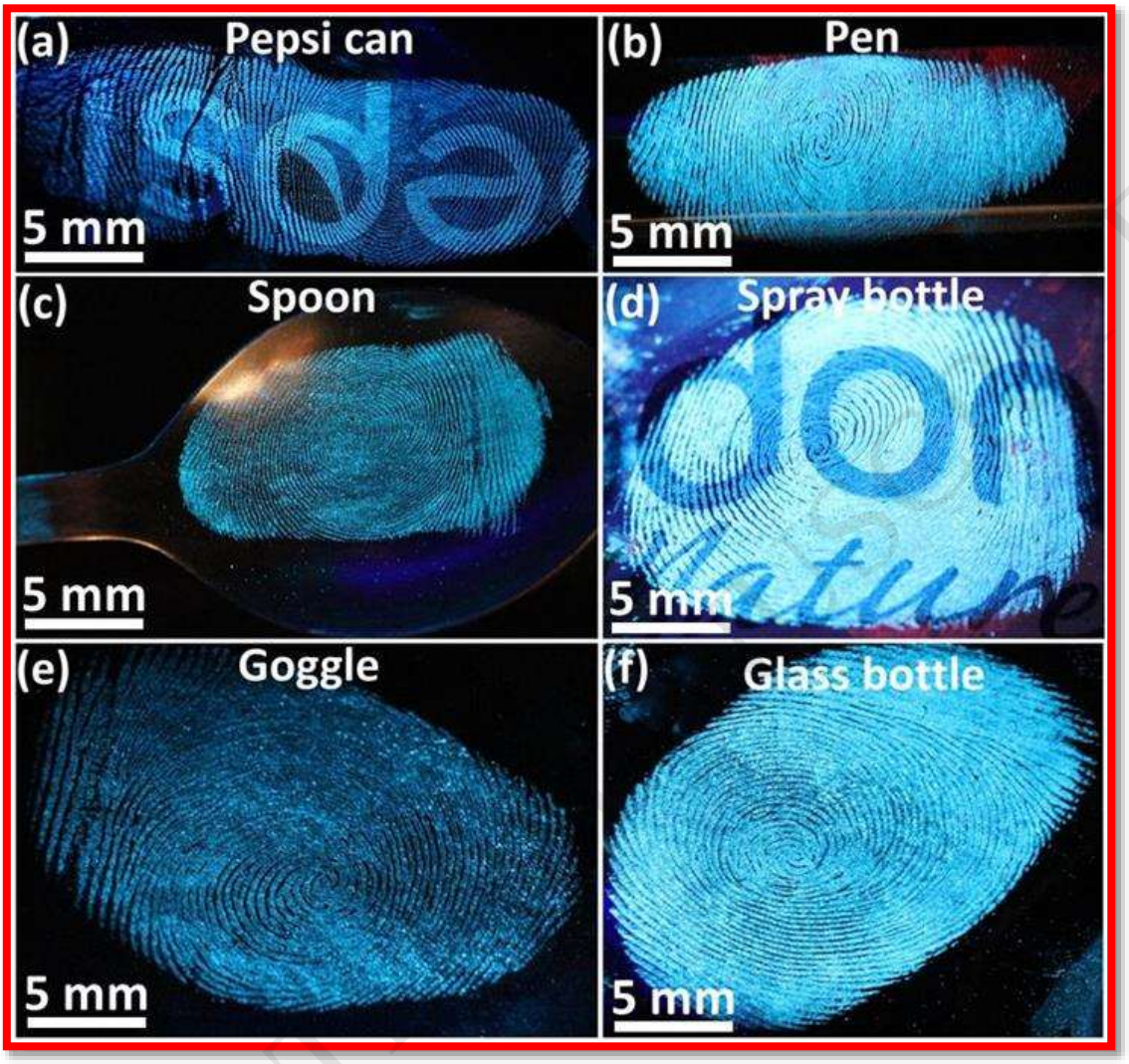

Fig.7. LFPs visualized by $GdAlO_3:Ce^{3+}$ (5 mol %) NPs on various curved surfaces, including (a) Pepsi can, (b) pen, (c) spoon, (d) spray bottle, (e) goggle and (f) glass bottle under UV 254 nm light.

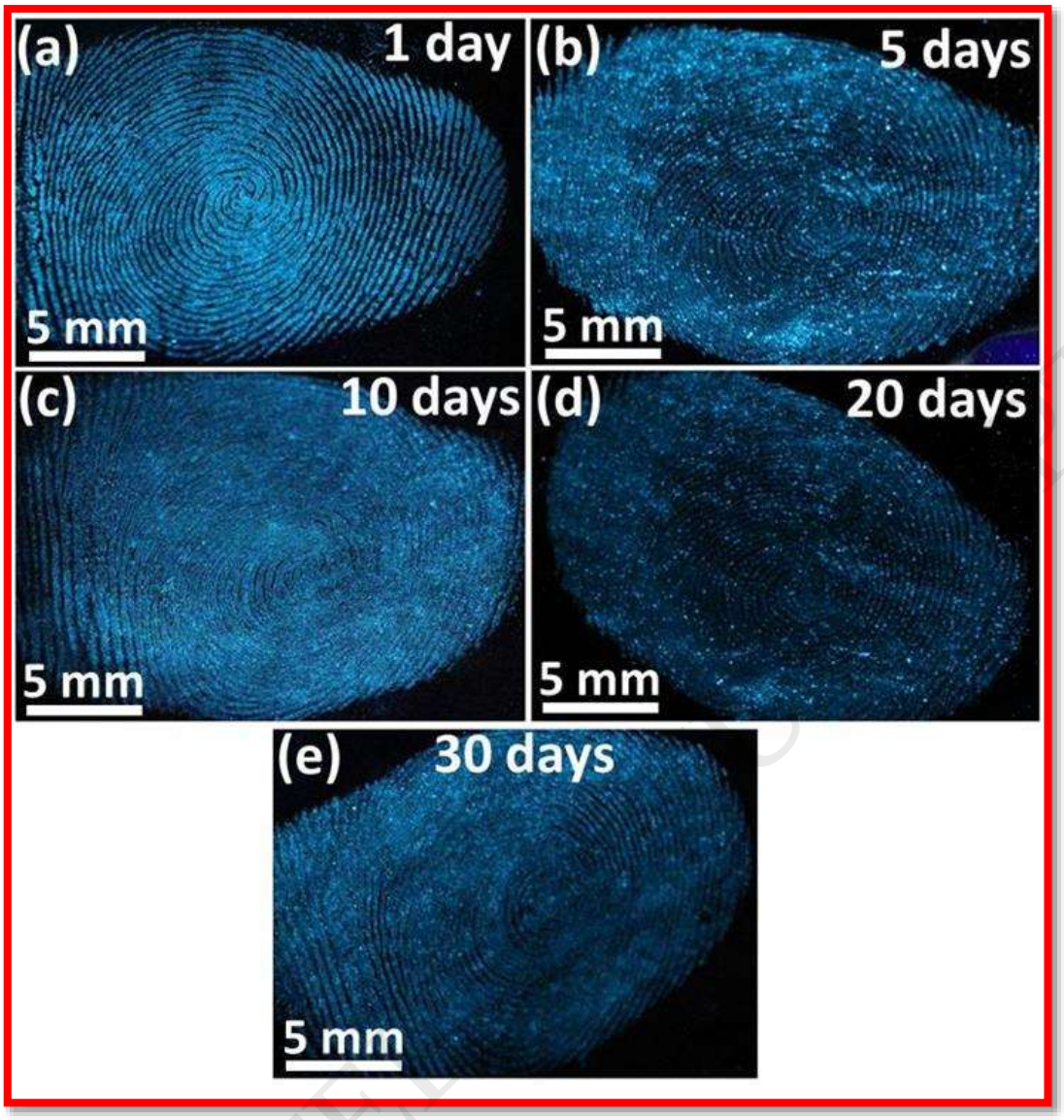

Fig.8. Digital photographs of LFPs stained with optimized NPs on the aluminum foil surface for various periods of time.

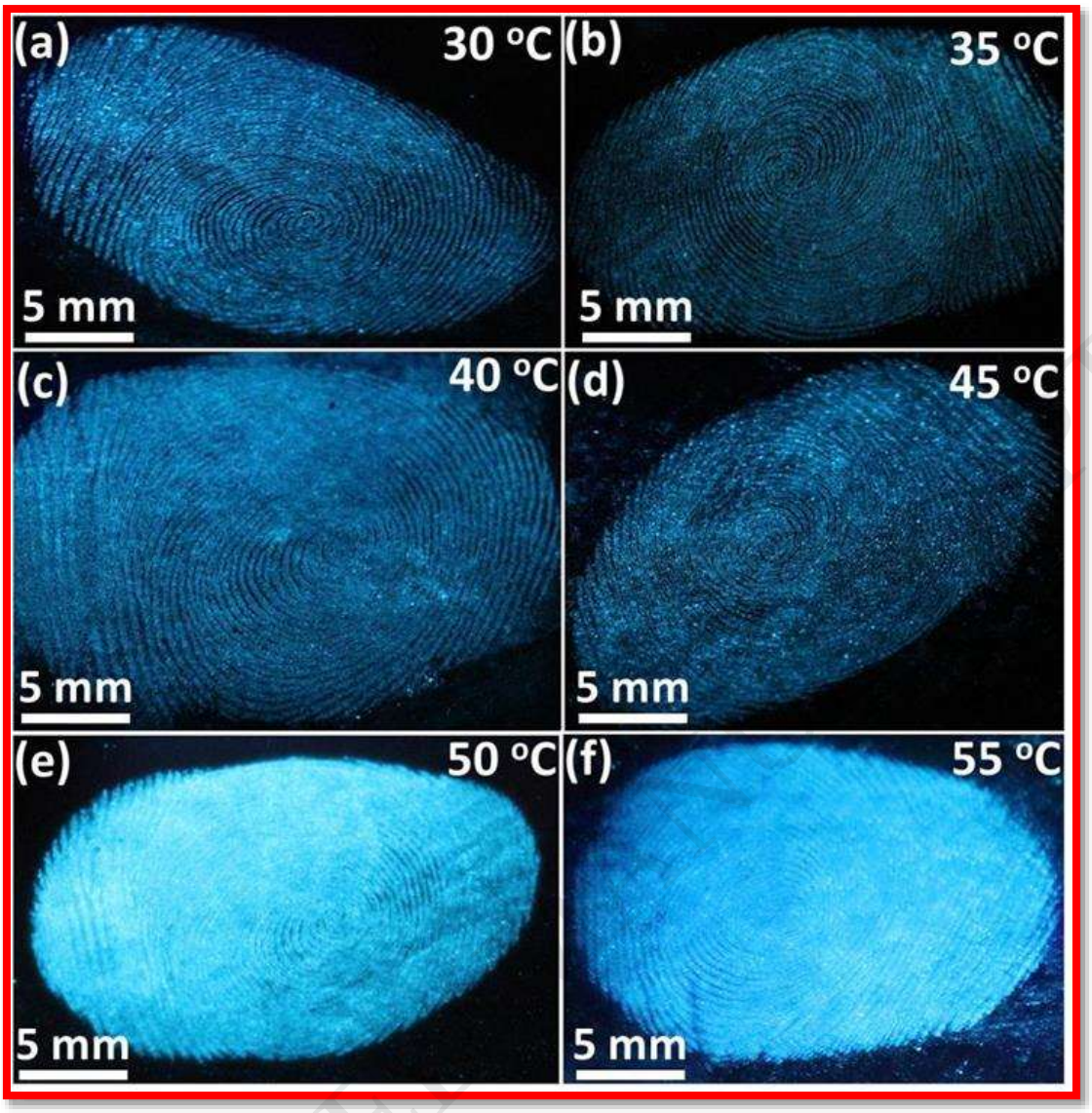

Fig.9. Photographed LFPs stained with $GdAlO_3:Ce^{3+}$ (5 mol %) NPs stored at different temperatures.

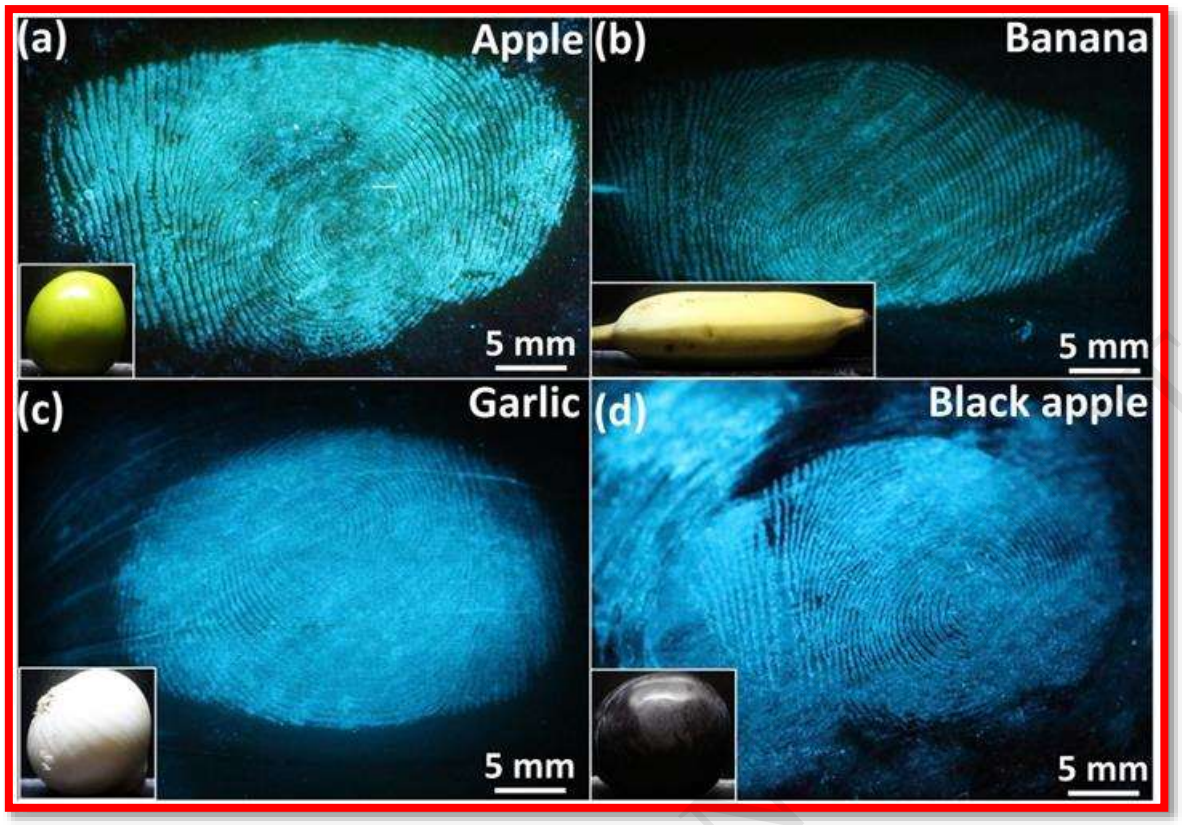

Fig.10. Visualized LFPs stained with $GdAlO_3:Ce^{3+}$ (5 mol %) NPs on various fruits and vegetable surfaces.

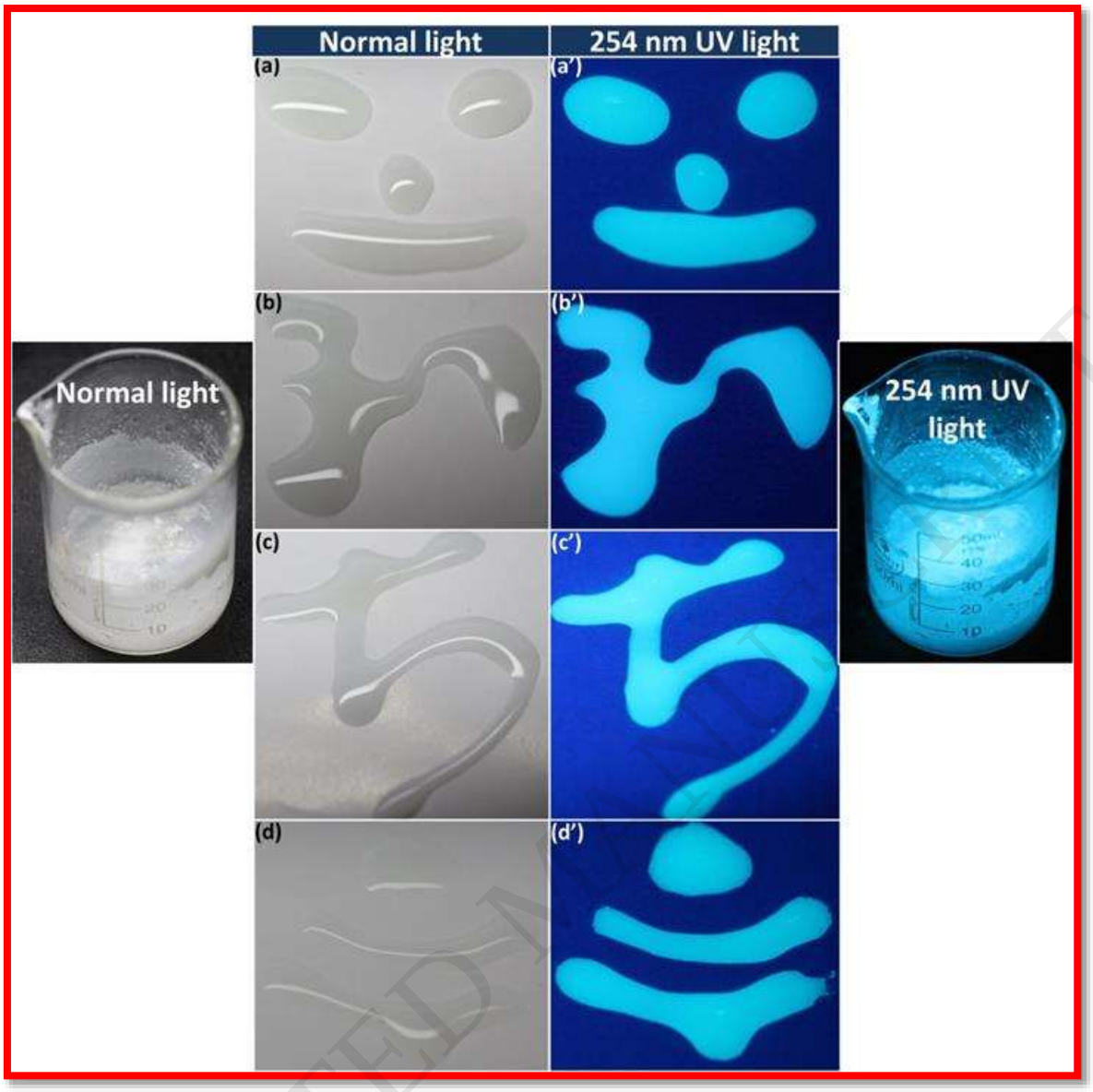

Fig.11. Anti-counterfeiting labels painted with $GdAlO_3:Ce^{3+}$ (5 mol %) NPs security ink under (a-d) normal light and (a'- d') UV light (254 nm).

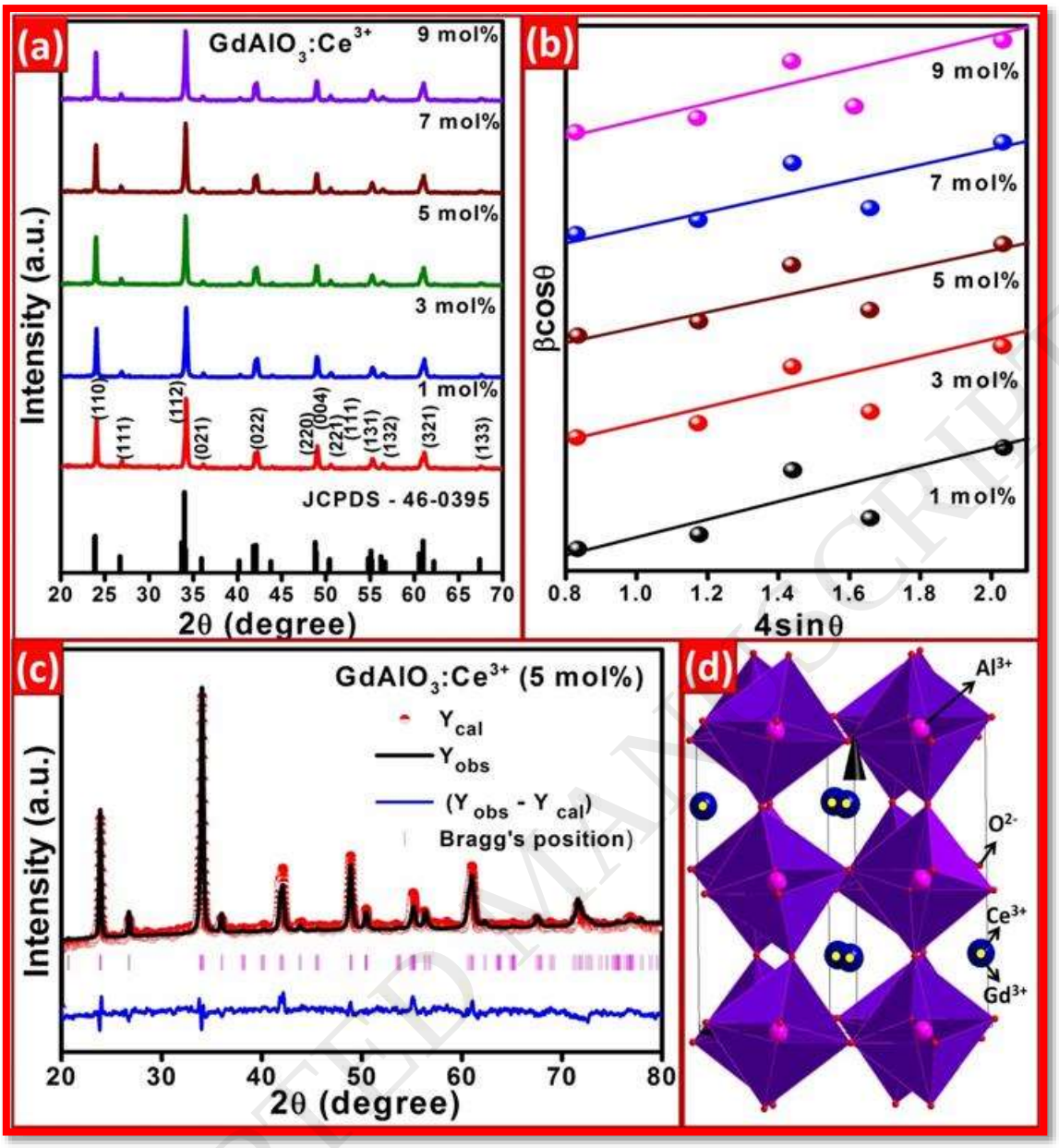

Fig.12 (a) PXRD patterns, (b) W-H plots, (c) Rietveld refinement and (d) packing diagram of $GdAlO_3:Ce^{3+}$ (5 mol %) NPs.

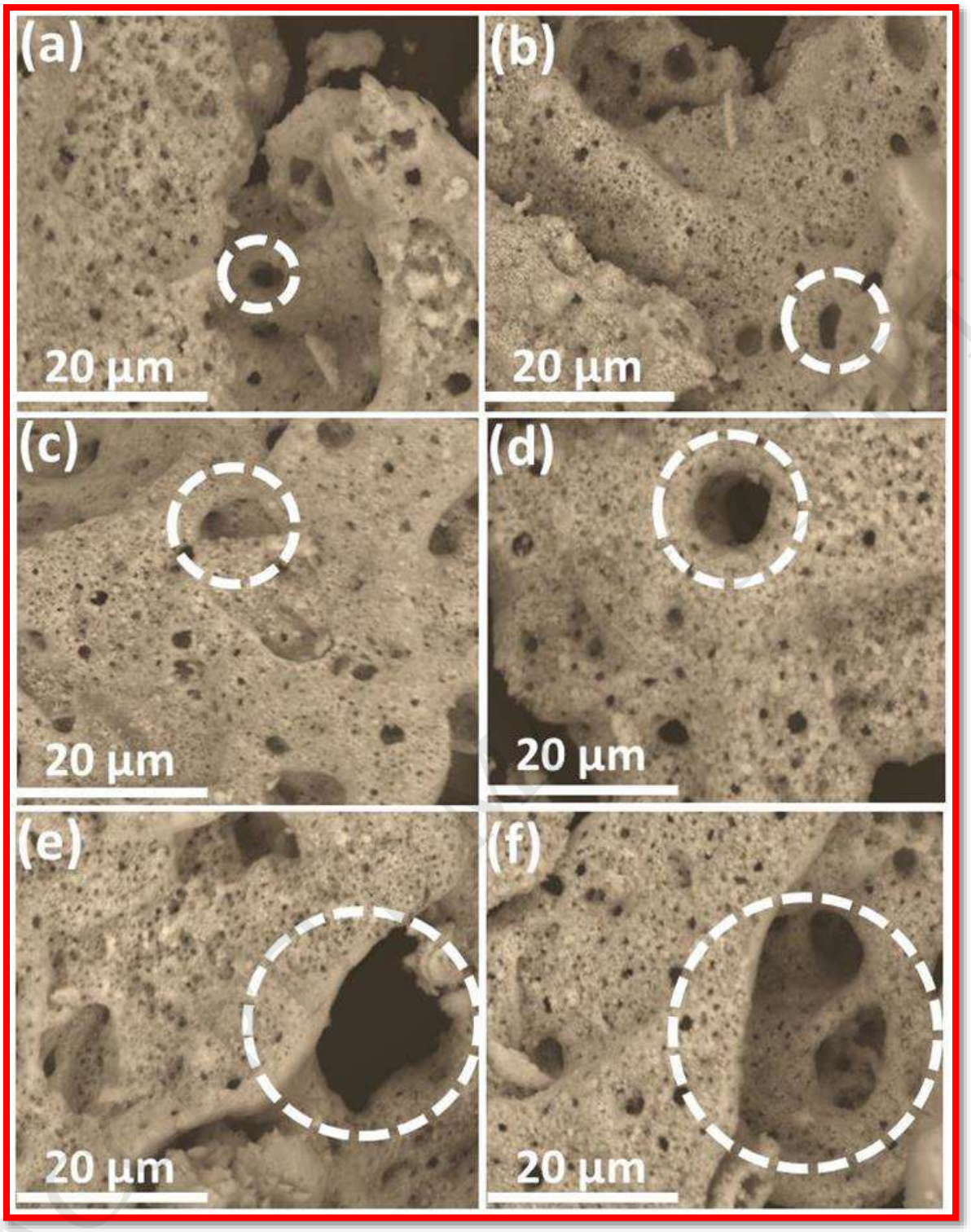

Fig.13. SEM micrographs of undoped and Ce^{3+} (1-9 mol %) doped $GdAlO_3$ NPs.

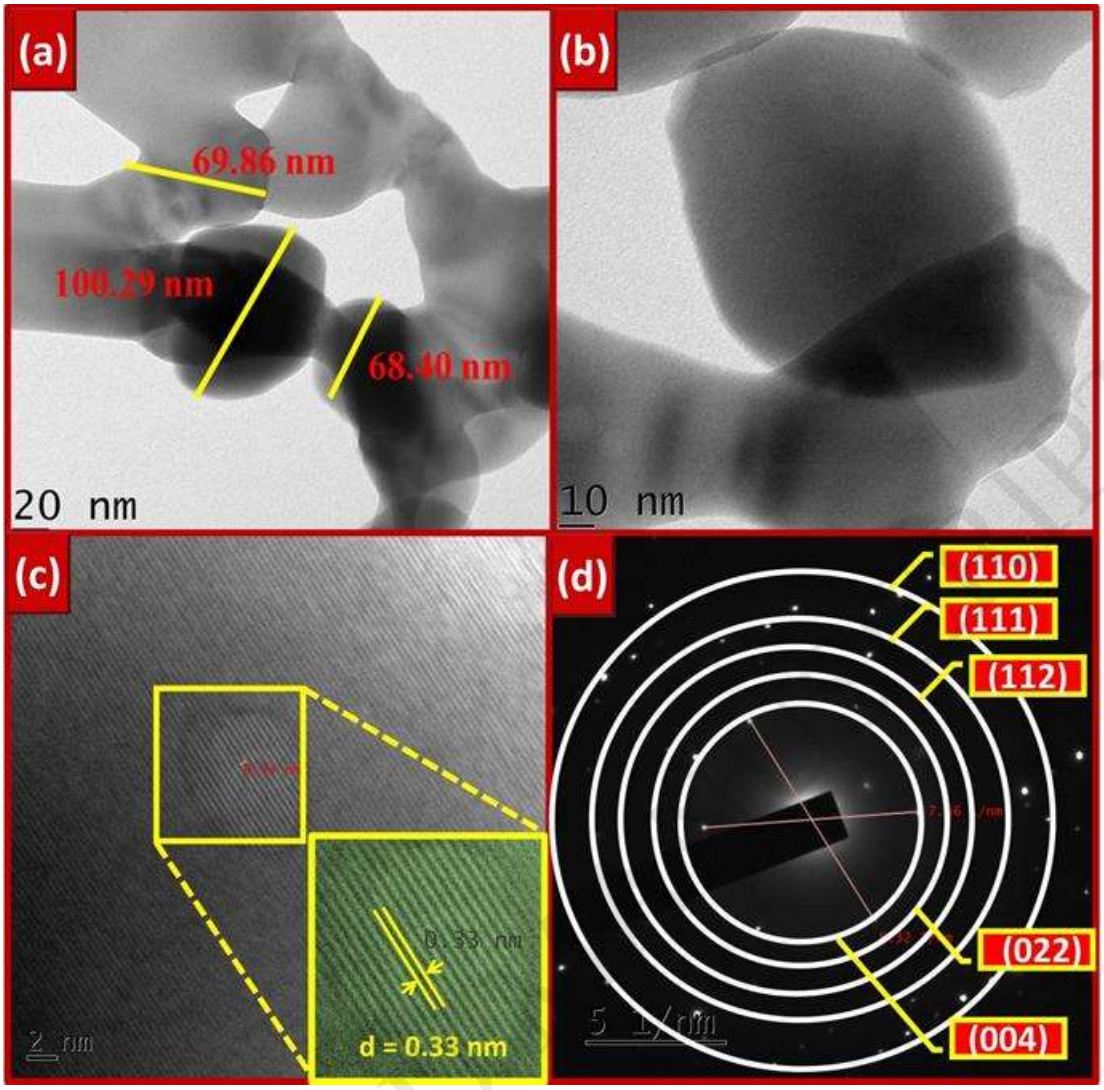

Fig.14 (a & b) TEM images, (c) HRTEM and (d) SAED patterns of $GdAlO_3:Ce^{3+}$ (5 mol %) NPs.

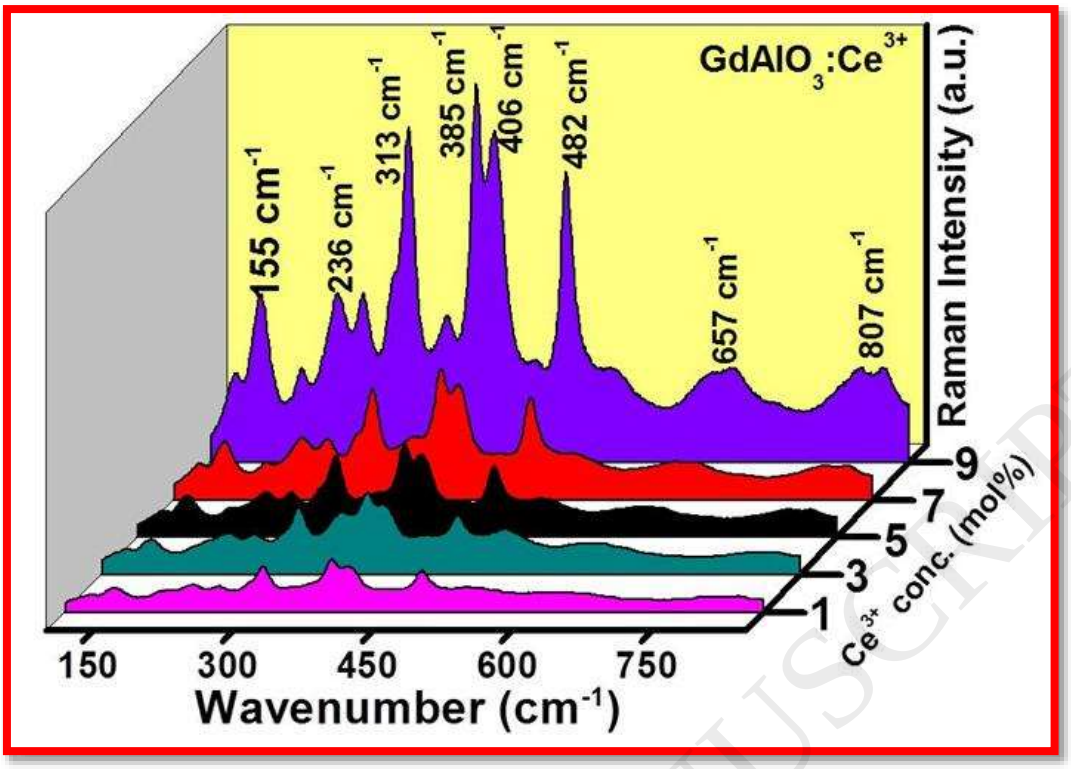

Fig.15. Raman spectra of $GdAlO_3:Ce^{3+}$ (1-9 mol %) NPs.

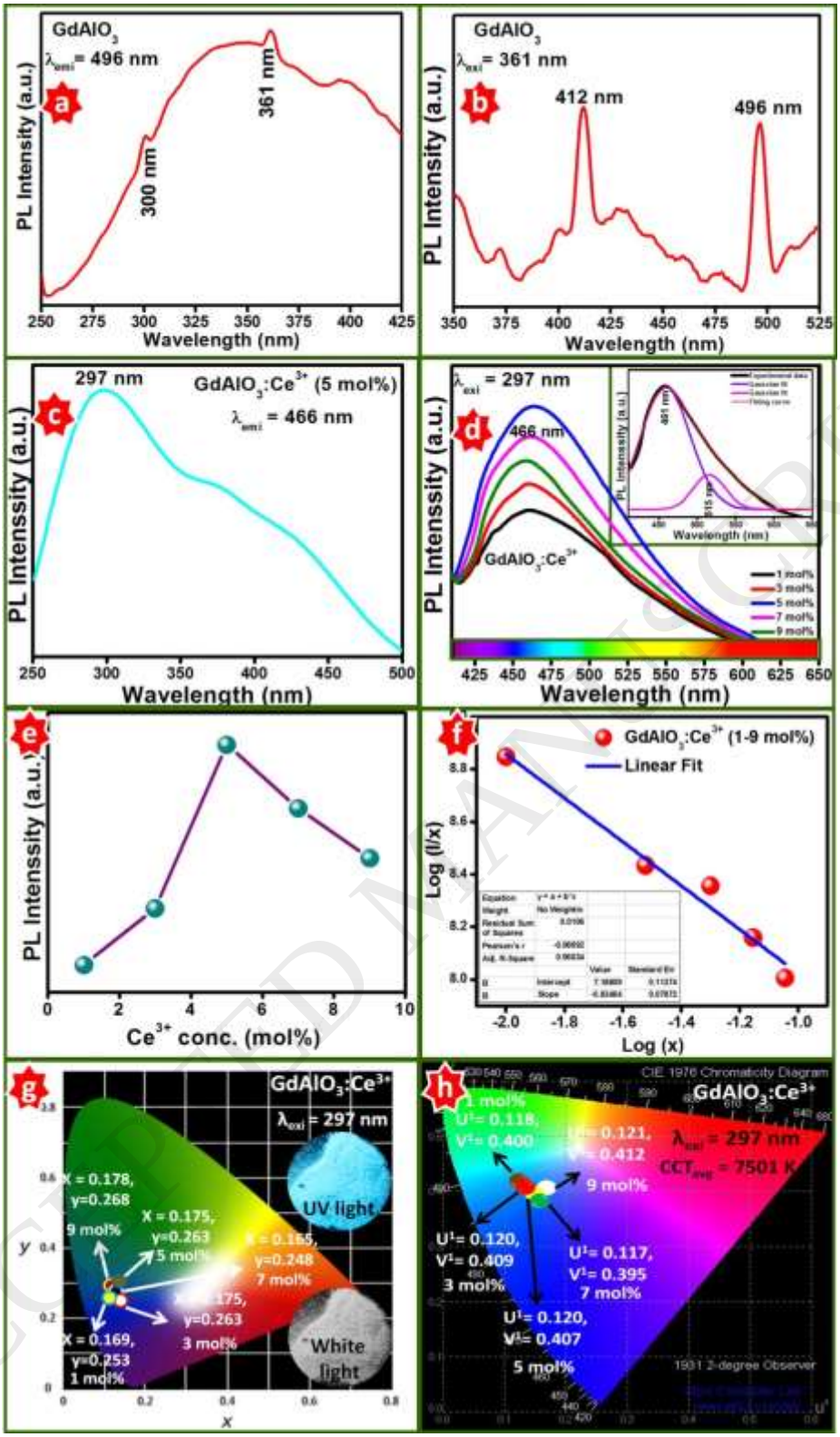

Fig.16 (a) Excitation spectrum and (b) emission spectra of undoped $GdAlO_3$, (c, d) excitation and emission spectra of $GdAlO_3:Ce^{3+}$ (1-9 mol %) NPs. (e) plot of variation of PL intensity with Ce^{3+} concentration, (f) log (x) vs log (I/x) plot, (g & h) CIE and CCT diagrams of $GdAlO_3:Ce^{3+}$ (1-9 mol %) NPs. [Inset: Deconvoluted spectrum of 466 nm emission peak].

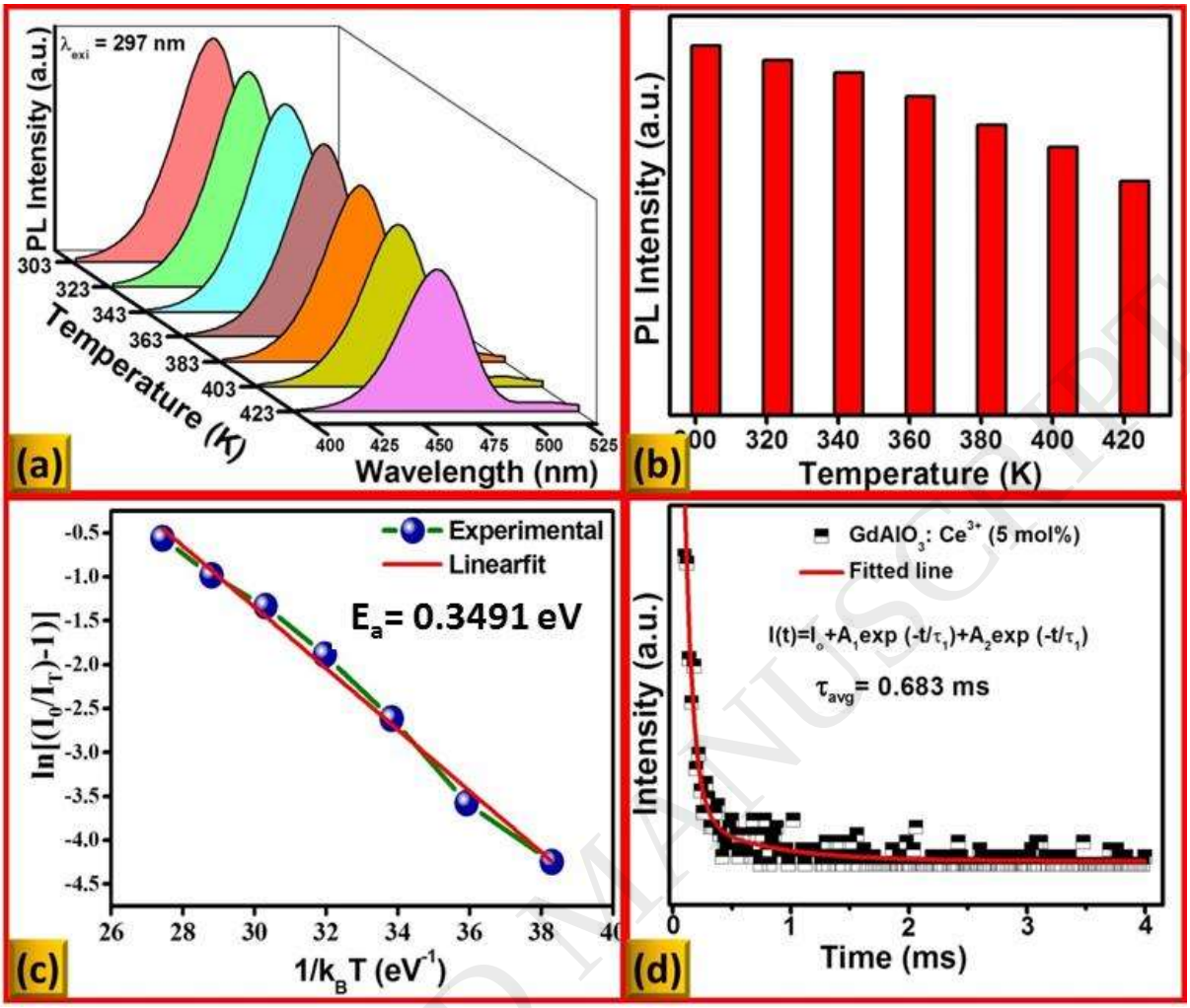

Fig.17 (a) Temperature dependent PL spectra, (b) variation of PL intensity versus temperature, (c) The plot of linear fitted curve of $\ln(I_0/I_T\text{-}1)$ versus $1/k_BT$ and (d) decay curves of $GdAlO_3:Ce^{3+}$ (5 mol %) NPs.

Table.1. Estimated crystallite size of $GdAlO_3:Ce^{3+}$ (1-9 mol %) NPs by Scherrer's and W-H plots method.

Ce^{3+} Conc. (mol %)	**Crystallite size (nm)**	
	Scherrer's method	**W–H plots**
1	56	54
3	65	60
5	67	63
7	74	71
9	76	73

Table.2. Structural parameters of un-doped and $GdAlO_3:Ce^{3+}$ (5 mol %) NPs obtained by Rietveld refinement.

Compound	**$GdAlO_3$**	**$GdAlO_3:Ce^{3+}$ (5 mol %)**
Crystal structure	Orthorhombic	Orthorhombic
Space group	*Pbnm*(No. 62)	*Pbnm* (No. 62)
Lattice Parameters (Å)		
a	5.2580(9)	5.2536(8)
b	5.3047(9)	5.2991(8)
c	7.4538(8)	7.4468(9)
Cell Volume ($Å^3$)	207.87(6)	207.42(6)
$R_{Factors}$		
R_p	8.68	8.54
R_{wp}	11.80	11.92
R_{exp}	12.64	13.11
χ^2	0.732	0.714
R_{Bragg}	5.85	5.78
R_F	5.36	5.24

Table.3. CIE, CCT and CP values of $GdAlO_3:Ce^{3+}$ (1-9 mol %) NPs.

Ce^{3+} Conc. (mol %)	CIE		CCT		CCT (K)	CP (%)
	X	Y	U'	V'		
1	0.169	0.253	0.1185	0.4004	7850	72
3	0.175	0.265	0.1201	0.4092	7459	75
5	0.175	0.263	0.1207	0.4078	7792	83
7	0.165	0.248	0.1175	0.3958	7129	78
9	0.178	0.268	0.1218	0.4121	7275	76

Table.4. PL decay life time of $GdAlO_3:Ce^{3+}$ (1-9 mol %) NPs.

Ce^{3+} Conc. (mol %)	**Life time parameters**		
	λ_{emi} = 466 nm, λ_{exi} = 297 nm		
	τ_1 (ms)	**τ_2 (ms)**	**τ_{avg} (ms)**
1	0.2454	0.7894	0.7104
3	0.2135	0.7583	0.6783
5	0.1983	0.7932	0.6745
7	0.2084	0.7471	0.6341
9	0.1500	0.7412	0.6275